



University of Maribor

Faculty of Energy Technology

# Journal of ENERGY TECHNOLOGY



Volume 14 / Issue 1

APRIL 2021

[www.fe.um.si/en/jet.html](http://www.fe.um.si/en/jet.html)



# Journal of ENERGY TECHNOLOGY



**VOLUME 14 / Issue 1**

Revija Journal of Energy Technology (JET) je indeksirana v bazah INSPEC© in Proquest's Technology Research Database.

The Journal of Energy Technology (JET) is indexed and abstracted in database INSPEC© and Proquest's Technology Research Database.



# JOURNAL OF ENERGY TECHNOLOGY

## Ustanovitelj / FOUNDER

Fakulteta za energetiko, UNIVERZA V MARIBORU /  
FACULTY OF ENERGY TECHNOLOGY, UNIVERSITY OF MARIBOR

## Izdajatelj / PUBLISHER

Fakulteta za energetiko, UNIVERZA V MARIBORU /  
FACULTY OF ENERGY TECHNOLOGY, UNIVERSITY OF MARIBOR

## Glavni in odgovorni urednik / EDITOR-IN-CHIEF

Jurij AVSEC

## Souredniki / CO-EDITORS

Bruno CVIKL  
Miralem HADŽISELIMOVIĆ  
Gorazd HREN  
Zdravko PRAUNSEIS  
Sebastijan SEME  
Bojan ŠTUMBERGER  
Janez USENIK  
Peter VIRTIC  
Ivan ŽAGAR

## Uredniški odbor / EDITORIAL BOARD

**Dr. Anton BERGANT,**  
Litostroj Power d.d., Slovenia

**Izr. prof. dr. Marinko BARUKČIĆ,**  
Josip Juraj Strossmayer University of Osijek, Croatia

**Prof. dr. Goga CVETKOVSKI,**  
Ss. Cyril and Methodius University in Skopje, Macedonia

**Prof. dr. Nenad CVETKOVIĆ,**  
University of Nis, Serbia

**Prof. ddr. Denis ĐONLAGIĆ,**  
University of Maribor, Slovenia

**Doc. dr. Brigita FERČEC,**  
University of Maribor, Slovenia

**Prof. dr. Željko HEDERIĆ,**  
Josip Juraj Strossmayer University of Osijek, Croatia

**Prof. dr. Marko JESENIK,**  
University of Maribor, Slovenia

**Izr. prof. dr. Ivan Aleksander KODELI,**  
Jožef Stefan Institute, Slovenia

**Izr. prof. dr. Rebeka KOVAČIČ LUKMAN,**  
University of Maribor, Slovenia

**Prof. dr. Milan MARČIČ,**  
University of Maribor, Slovenia

**Prof. dr. Igor MEDVED,**  
Slovak University of Technology in Bratislava, Slovakia

**Izr. prof. dr. Matej MENCINGER,**  
University of Maribor, Slovenia

**Prof. dr. Greg NATERER,**  
Memorial University of Newfoundland, Canada

**Prof. dr. Enrico NOBILE,**  
University of Trieste, Italia

**Prof. dr. Urška LAVRENČIČ ŠTANGAR,**  
University of Ljubljana, Slovenia

**Izr. prof. dr. Luka SNOJ,**  
Jožef Stefan Institute, Slovenia

**Izr. prof. dr. Simon ŠPACAPAN,**  
University of Maribor, Slovenia

**Prof. dr. Gorazd ŠTUMBERGER,**  
University of Maribor, Slovenia

**Prof. dr. Anton TRNIK,**  
Constantine the Philosopher University in Nitra, Slovakia

**Prof. dr. Zdravko VIRAG,**  
University of Zagreb, Croatia

**Prof. dr. Mykhailo ZAGIRNYAK,**  
Kremenchuk Mykhailo Ostrohradskiy National University, Ukraine

**Prof. dr. Marija ŽIVIĆ,**  
University of Slavonski Brod, Croatia

**Tehnični urednik / TECHNICAL EDITOR**

Sonja Novak

**Tehnična podpora / TECHNICAL SUPPORT**

Tamara BREČKO BOGOVČIČ

**Izhajanje revije / PUBLISHING**

Revija izhaja štirikrat letno v nakladi 100 izvodov. Članki so dostopni na spletni strani revije - [www.fe.um.si/si/jet.html](http://www.fe.um.si/si/jet.html) / The journal is published four times a year. Articles are available at the journal's home page - [www.fe.um.si/en/jet.html](http://www.fe.um.si/en/jet.html).

Cena posameznega izvoda revije (brez DDV) / Price per issue (VAT not included in price): 50,00 EUR

Informacije o naročninah / Subscription information: <http://www.fe.um.si/en/jet/subscriptions.html>

**Lektoriranje / LANGUAGE EDITING**

Terry T. JACKSON

**Oblikovanje in tisk / DESIGN AND PRINT**

Fotografika, Boštjan Colarič s.p.

**Naslovna fotografija / COVER PHOTOGRAPH**

Jurij AVSEC

**Oblikovanje znaka revije / JOURNAL AND LOGO DESIGN**

Andrej PREDIN

**Ustanovni urednik / FOUNDING EDITOR**

Andrej PREDIN

---

Izdajanje revije JET finančno podpira Javna agencija za raziskovalno dejavnost Republike Slovenije iz sredstev državnega proračuna iz naslova razpisa za sofinanciranje domačih znanstvenih periodičnih publikacij / The Journal of Energy Technology is co-financed by the Slovenian Research Agency.

## ***Spoštovani bralci revije Journal of energy technology (JET)***

Energija vetra je posledica obsevanja Zemljine površine s sončnimi žarki. Potenciali vetrne energije v svetu so zelo veliki, mnogo večji kot trenutno izkoriščanje energije vetra. Intenzivnost vetrne energije je geografsko različna, pravzaprav pa ni države oz. pokrajine, kjer ni območij s potenciali za izkoriščanje. Tovrstno energijo so znali izkoriščati že v preteklosti; tako naj bi že 5000 let pred našim štetjem uporabljali vetrno energijo za pogon ladij vzdolž reke Nil, pred približno 200 leti pred našim štetjem pa so jo Kitajci uporabljali za pogon enostavnih črpalk. Uporaba energije vetra se je nato razširila. Tako so ljudje na ozemlju srednjega vzhoda v 11. stoletju že uporabljali energijo vetra za pogon vetrnih črpalk in vetrnih mlinov. Še posebej velikopotezna je bila uporaba vetrne energije na Nizozemskem za izsuševanje potiskanja morja.

Danes predstavlja vetrna energija v svetu zelo pomemben člen v proizvodnji električne energije. V letu 2020 imajo inštalirane vetrne elektrarne moč že preko 750 GW. Globalno največ energije izkoriščajo na Kitajskem, v ZDA in Nemčiji. Največ električne energije na prebivalca pridobijo na Danskem, Švedskem, Irskem in v Nemčiji. Največje vetrne elektrarne imajo moč okoli 10 MW, s premeri rotorjev okoli 160 m. V Sloveniji je izraba vetrne energije za proizvodnjo električne energije zelo majhna, prav zato so raziskave na tem področju izjemnega pomena. Vsekakor je potrebno v bližnji prihodnosti v energetiki dati večji poudarek izrabi vetrne energije. V tej številki revije je predstavljen članek na to tematiko, zato vas vabim k branju revije.

Jurij AVSEC  
odgovorni urednik revije JET

## ***Dear Readers of the Journal of Energy Technology (JET)***

Wind energy results from the irradiation of the Earth's surface with solar rays. The global potential of wind energy is massive, much greater than the current exploitation of it. The intensity of wind energy is geographically different, but there is no country or province in the world without areas with interesting potentials for wind energy. People have known how to harness the power of the wind since ancient times; Egyptians used wind energy to power ships along the Nile 5,000 years BC, and about 200 BC the Chinese used wind energy to power simple pumps. The use of wind energy then spread worldwide; in the 11th century, people in the Middle East used wind energy to power wind pumps and windmills. The use of wind energy in the Netherlands to recover land from the sea was particularly ambitious.

Today, wind energy is an essential link in global electricity production. In 2020, the installed wind power plants had a capacity of over 750 GW. China, the United States and Germany produce the most energy. Denmark, Sweden, Ireland and Germany have the most electricity per capita from wind energy. The largest wind farms have a capacity of about 10 MW, with rotor diameters of about 160m. In Slovenia, the use of wind energy for electricity production is very small, which is why research in this field is extremely important. In any case, greater emphasis needs to be placed on the use of wind energy in the near future. This issue of the magazine presents an article on this very topic, so I invite readers to read further.

Jurij AVSEC  
Editor-in-chief of JET

# ***Table of Contents / Kazalo***

<b>New technique to evaluate the overall heat loss coefficient for a flat plate solar collector</b> Nova tehnika za oceno celotnega koeficienta toplotne izgube za ploščati sončni kolektor	
<b>Amor Bouhdjar, Hakim Semai, Aissa Amari . . . . .</b>	<b>.11</b>
<b>Towards Forty Years of Krško NPP Operation – An Overview of Population Exposures to Radiation</b> Ob koncu četrtega desetletja delovanja ne Krško - pregled sevalne izpostavljenosti prebivalstva	
<b>Matjaž Koželj . . . . .</b>	<b>.27</b>
<b>Comparison of cavitation models for the prediction of cavitation around a hydrofoil</b> Primerjava kavitacijskih modelov za numerično napoved kavitacije na hidrodinamičnem profilu	
<b>Marko Pezdevšek, Ignacijo Biluš, Gorazd Hren . . . . .</b>	<b>.41</b>
<b>Modelling of magnetic regenerator and heat transfer agent microchannels</b> Modeliranje magnetnega regeneratorskega sredstva za prenos toplote v mikrokanalih	
<b>Dorin Botoc, Bianca-Eliza Oneata, Ionut Rusu, Alexandru Salceanu, Jurij Avsec. . . . .</b>	<b>.57</b>
<b>Instructions for authors . . . . .</b>	<b>.69</b>

# NEW TECHNIQUE TO EVALUATE THE OVERALL HEAT LOSS COEFFICIENT FOR A FLAT PLATE SOLAR COLLECTOR

## NOVA TEHNIKA ZA OCENO CELOTNEGA KOEFIČIENTA TOPLOTNE IZGUBE ZA PLOŠČATI SONČNI KOLEKTOR

Amor Bouhdjar<sup>1,✉</sup>, Hakim Semai<sup>1</sup>, Aissa Amari<sup>1</sup>

**Keywords:** flat plate solar collector, overall heat loss coefficient, heat removal factor

### **Abstract**

Low-temperature solar systems mostly use flat plate solar collectors. Good design and correct dimensioning of a solar heat generator are based on precise knowledge of the characteristics of the flat plate solar collector on site. The present work considers a flat plate solar air collector, a flat plate solar water collector, and a flat plate solar water collector with air absorber cooling. The investigation intends to shed light on a procedure to determine the overall heat loss coefficient and the heat removal factor using recorded system temperatures, operating parameters, and environmental data. The Hottel-Whillier-Bliss equation gives the collector useful energy. This expression is used to generate a correlation for the collector efficiency through a linear fitting. We calculate the overall heat loss coefficient of the collector from the slope of the collector efficiency curve. However, we need to know the heat removal factor of the collector. In this study, we present a new technique to calculate the heat removal factor. Then we deduce the collector overall heat loss coefficient.

Results show that, very often, the overall heat loss coefficient for the flat plate solar air collector and the flat plate solar water collector determined with this new method is higher than the one calculated with the empirical formula proposed by Klein.

<sup>✉</sup> Corresponding author: Dr Amor Bouhdjar, Tel.: +231 (0) 23189051, mailing address: PB. 62 Route de l'Observatoire Bouzareah 16340 Algiers Algeria, E-mail address: [a\\_bouhdjar@yahoo.com](mailto:a_bouhdjar@yahoo.com); [a.bouhdjar@cder.dz](mailto:a.bouhdjar@cder.dz)

<sup>1</sup>Renewable Energy Development Centre, Solar thermal and Geothermal Energy Division, Route de l'Observatoire Bouzareah 16340 Algiers Algeria

However, the experimental overall heat loss coefficient for the flat plate solar water collector with air absorber cooling is smaller than the one calculated with the empirical formula proposed by Klein. The analysis shows that the overall heat loss coefficient determined with the new technique seems more realistic since all phenomena occurring during the heat transfer from solar irradiance incident on the absorber plate and transmitted to the transport fluid are considered.

## **Povzetek**

Nizkotemperaturni sončni sistemi večinoma uporabljajo sončne kolektorje z ravno ploščo. Dobra zasnova in pravilne dimenzije solarne generatorja toplote temeljijo na natančnem poznavanju značilnosti ploščatega sončnega kolektorja na lokaciji. Pričujoče delo obravnava ravno zračni ploščati sončni kolektor, vodni ploščati sončni kolektor in ploščasti sončni kolektor vode z zračnim absorberjem. Analiza v članku namerava osvetliti postopek določanja celotnega koeficienta toplotnih izgub in faktorja odvajanja toplote z uporabo zabeleženih temperatur sistema, obratovalnih parametrov in okoljskih podatkov. Enačba Hottel-Whillier-Bliss daje raziskovalcem koristne informacije. Ta izraz se uporablja za ustvarjanje korelacije za učinkovitost kolektorja z linearno vgradnjo. Skupni koeficient toplotnih izgub kolektorja izračunamo iz naklona krivulje izkoristka kolektorja. Poznati pa moramo faktor odvajanja toplote kolektorja. V tej študiji predstavljamo novo tehniko za izračun faktorja odvajanja toplote. Nato izračunamo koeficient celotne toplotne izgube kolektorja.

Rezultati kažejo, da je skupni koeficient toplotne izgube za ravno ploščasti zračni sončni kolektor in vodni ploščati sončni kolektor, določen s to novo metodo, večji od tistega, izračunanega z empirično formulo, ki jo je predlagal Klein.

Vendar je eksperimentalni skupni koeficient toplotne izgube za vodni ploščati sončni kolektor z zračnim absorberjem manjši od tistega, izračunanega z empirično formulo, ki jo je predlagal Klein. Analiza kaže, da se zdi skupni koeficient toplotne izgube, določen z novo enačbo, bolj realen, saj so upoštevani vsi pojavi, ki se pojavijo med prenosom toplote zaradi sončnega obsevanja, ki vpade na ploščo absorberja in se prenese v transportno tekočino.

## **1 INTRODUCTION**

With the trend of decarbonization, many countries are moving toward using alternative energy sources such as solar, wind, biomass, geothermal, and others. For the supply of heat, solar water heating systems (SWHS) are widely used, especially in countries with good solar radiation. These systems are sufficiently mature to replace gas and other fossil fuel to supply heat in domestic or industrial applications. Solar air collectors are also integrated into many heating systems such as air space heating, drying applications, such as agricultural products, timber, biomass cultivation, waste biomass, building materials and desalination, and regulating microclimate in agricultural products storage facilities. Improvement of system efficiency and managerial flexibility of the energy obtained can expand the use of solar energy. In a scenario still characterized by strong growth in the installed solar collector capacity, [1], even relatively small improvements may lead to a large increase in the overall energy production in absolute terms. Rigorous studies may also lead to adequate provisions.

For this reason, research and development into the optimization of the collector characteristics and solar field design play key roles. Flat plate solar collectors (FPSC) are the main and most used solar water heating systems component. It is made of an absorber plate covered above by a

transparent sheet and surrounded by an isolating material. Incident solar radiations onto the absorber are absorbed by the latter and transferred as heat to a fluid flowing within the absorber. Therefore, a flat plate solar water collector is a special type of heat exchanger.

In contrast, a flat plate solar air collector (FPSAC) is a simple solar heating system with a low convective heat transfer coefficient between the absorber surface and the flowing air, resulting in a low heat transfer rate. Low thermal conductivity of air and high heat loss to the environment are the drawbacks of solar air collectors, [2, 3]. Solar thermal flat plate collector performance depends very much on the absorbed solar radiation and the energy lost to the environment.

Many authors have examined various configurations to assess the influence of geometrical characteristics and operating conditions on the thermal efficiency of flat plate solar water collectors. Important parameters such as absorber thickness, riser position, the shape of the tube's cross-section, plate material, coating effect on absorptivity, cover transmissivity, fluid properties, and mass flow rate were investigated [4]. Other studies investigate cover absorber distance, heat transfer between absorber plate and cover sheet, the roughness of absorber plate surface, or use of transparent insulation material, [5].

Lowering heat losses from the absorber to the surrounding environment is an important issue for FPSC. The use of selective coating techniques was an innovation to reduce thermal radiation heat transfer from the absorber while maintaining high plate absorptivity, [6]. Others investigated heat convection between the glass cover and absorber plate and the influence of the distance between these two components, [7].

Several other studies have been made on flat plate solar water heaters, [8-11], mainly on the determination of the global heat loss coefficient and the heat removal factor of the collector. Klein, [12], proposed a mathematical model, based on the theory of Bliss-Whillier, [13, 14], which estimates the collector efficiency factor and the heat removal factor of the collector considering many simplifying assumptions. The performance of solar air collectors is usually affected by the low heat transfer coefficient between the air and the absorber plate, [10]. The choice of the optimal collector depends on the temperature level required by the specific application and on the climatic conditions at the installation site. Therefore, in terms of efficiency, each collector displays features, making it most suitable to a given application. Several new applications of solar energy have appeared and intensified their use, as shown by works developed by Esen, [15, 16].

Efforts have been made to combine a number of the most important factors into a single formulation to have a mathematical model, which will describe the collector's thermal performance in a computationally efficient manner. Evaluating the thermal loss coefficients is the fundamental task to assess the flat plate solar collector performance. The FPSC global heat loss coefficient  $U_c$  ( $W/m^2.K$ ) is the sum of the top loss ( $U_t$ ), the bottom loss ( $U_b$ ), and the edge loss ( $U_e$ ) coefficients. This loss value is established between the collector and its surrounding by conduction, infrared solar radiation, and convection heat transfer. A good approximation of the FPSC global heat loss coefficient will lead to an effective solar water system design.

The present work aims to determine the overall loss heat coefficient of the flat plate solar collector using a new technique to evaluate the heat removal factor of the collector, taking into consideration experimental data to minimize the effect of assumptions made in other studies. This more realistic deduced overall heat loss coefficient will be compared to the one obtained by the Klein empirical formula, [12].

## 2 SYSTEM THEORY

Under steady-state conditions, the collector delivers a useful energy rate ( $Q_u$ ) equal to the rate of radiation energy absorbed by the collector minus the energy rate transmitted to its surroundings.

$$Q_u = A_c [I_c(\tau\alpha) - U_c(T_p - T_a)] = \dot{m}C_p [T_o - T_i] \quad (2.1)$$

After some reshuffling, it becomes, [17]:

$$Q_u = A_c F_R [I_c(\tau\alpha) - U_c(T_i - T_a)] \quad (2.2)$$

with  $F_R$ , the heat removal factor that is determined by:

$$F_R = \frac{\dot{m}C_p(T_o - T_i)}{A_c [I_c(\tau\alpha) - U_c(T_i - T_a)]} \quad (2.3)$$

The collector efficiency is given by:

$$\eta = \frac{Q_u}{A_c I_c} = F_R \left[ (\tau\alpha) - \frac{U_c(T_i - T_a)}{I_c} \right] \quad (2.4)$$

Which is equivalent to:

$$\eta = \frac{\dot{m}C_p(T_o - T_i)}{I_c A_c} \quad (2.5)$$

Equations (2.4) and (2.5) will let us draw the efficiency curve versus  $\frac{(T_i - T_a)}{I_c}$  from experimental data.

Transforming equation (2.2), we obtain:

$$Q_u = F_R Q_u + A_c F_R U_c (T_p - T_i) \quad (2.6)$$

From equation (2.6), we obtain the temperature difference between the absorber temperature and the fluid inlet temperature:

$$T_p - T_i = \frac{Q_u}{A_c F_R U_c} (1 - F_R) \quad (2.7)$$

Taking into consideration equation (2.4), we obtain:

$$F_R = \frac{\eta I_c}{I_c \tau\alpha - U_c(T_i - T_a)} \quad (2.8)$$

From equations (2.4) and (2.7), we obtain:

$$A_c F_R U_c = \eta A_c I_c \frac{(1 - F_R)}{T_p - T_i} \quad (2.9)$$

Combining equation (2.9) and equation (2.4), we obtain:

$$\eta = F_R \tau\alpha - \eta(1 - F_R)\theta \quad (2.10)$$

in which

$$\theta = \frac{T_i - T_a}{T_p - T_i} \quad (2.11)$$

From equation (2.10), we derive  $F_R$

$$F_R = \frac{\eta(1+\theta)}{\tau\alpha+\eta\theta} \quad (2.12)$$

We observe that  $F_R$  can be calculated based on physical parameters and operating parameters, including the absorber temperature, environment temperature and inlet fluid temperature. The collector efficiency coefficient is given by equation (2.4) and equation (2.5).

Considering the experimental data, we plot the efficiency coefficient versus  $\frac{(T_i-T_a)}{I_c}$ . From the slope ( $F_R U_C$ ) of the experimental curve  $\eta$  versus  $\frac{(T_i-T_a)}{I_c}$  we determine the overall experimental loss coefficient knowing that  $F_R$  can be determined by equation (2.12).

For comparison, we calculate the heat loss coefficient using the widely used empirical equation given by Klein, [12]:

$$U_t = \frac{1}{\frac{N_g}{\frac{C}{T_p} \left[ \frac{T_p - T_a}{N_g + f} \right]^{0.33} + \frac{1}{h_w}}} + \frac{\sigma(T_p^2 + T_a^2)(T_p + T_a)}{\frac{1}{\varepsilon_p + 0.05N_g(1 - \varepsilon_p)} + \frac{2N_g + f - 1}{\varepsilon_g} - N_g} \quad (2.13)$$

with

$$f = (1 - 0.04h_w + 0.0005h_w^2)(1 + 0.091N_g) \quad (2.14)$$

$$C = 365.9(1 - 0.00883\beta + 0.000129\beta^2) \quad (2.15)$$

$$h_w = \frac{8.6V^{0.6}}{L^{0.4}} \quad (2.16)$$

Due to a low bottom casing temperature, the radiative heat exchange with the surrounding can be neglected. Only the convection term is considered, [17]; thus, the heat transfer coefficient for the heat transmitted from the back to the surrounding is given by:

$$U_b = \frac{1}{\frac{t_b}{k_b} + \frac{1}{h_{c,b-a}}} \quad (2.17)$$

Similarly, the heat transfer coefficient for the heat transferred from the collector edges to the environment, still assuming that radiation heat transfer is negligible, is given by:

$$U_e = \frac{1}{\frac{t_e}{k_e} + \frac{1}{h_{c,e-a}}} \quad (2.18)$$

The overall heat loss coefficient for the collector is the sum of the heat loss coefficient for the top, the heat loss coefficient for the bottom, and the heat loss coefficient for the edges.

$$U'_c = U_t + U_b + U_e \quad (2.19)$$

Regarding the flat plate solar water collector with air absorber cooling, we replace the previous expression by the sum of heat rate for both fluids, and  $T_i$  takes the smallest inlet temperature from both fluids.

### 3 EXPERIMENTAL SET-UP

To determine the collector characteristics experimentally, primarily the overall heat loss coefficient, an experimental bench was set up (Fig.1). In the first configuration, a cross-section of the solar air collector shows a glass cover, an air gap between the glass cover and the absorber plate, the absorber plate fins, the air channel under the absorber, back and edge insulation and the casing.

In the second configuration, a cross-section of the solar water collector shows a glass cover, an air gap between the glass cover and the absorber plate, a grooved plate to which riser tubes are embedded, back and edge insulation and the casing. The third configuration is identical to the solar water collector to which an air channel is added between a finned absorber and the back insulation.

The used cover glass has low iron content in the three cases and is sealed to the casing with windshield silicone sealer. The absorber plate of 1 mm thickness is made of aluminium in the three cases. The absorber coating is matt black painting. In the second and third configurations, the embedded tube risers are made of copper. The back and the edges are insulated using rigid polyurethane panels.

The benches are instrumented with thermocouples type K to measure temperatures (cover, absorbing plate, inlet and outlet fluids, collector back, ambient, etc.). Air speed was measured using a hot wire CFM anemometer with 0.01m/s resolution. A Kipp and Zonen pyranometer mounted at the collector orientation is used to measure the global incident solar radiation. During the experiment, recorded parameters come under the required environment conditions (Table 1).

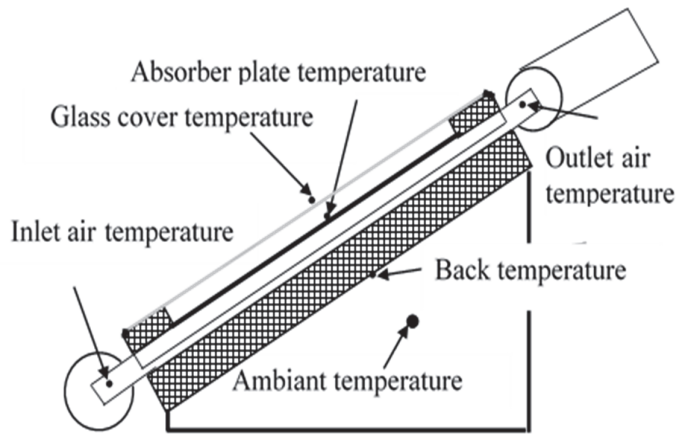
Physical properties of the materials were obtained from their documentation. All geometrical dimensions are given in the figures and Table 2. Airflow is generated with a centrifugal exhaust fan. In the case of the water collector, a water pump is used to perform forced circulation in the solar collector circuit. A flow meter is inserted in the water circuit in order to record the flow rate. Figure 2 shows the solar collectors constructed and used for the experiment.

**Table 1:** Required environmental conditions (ASHRAE 93)

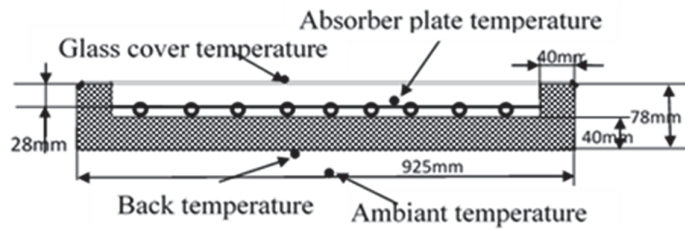
Variable	Absolute limits
<ul style="list-style-type: none"> <li>• Total solar irradiance normal to sun (<math>W/m^2</math>)</li> <li>• Diffuse fraction (%)</li> <li>• Wind speed (m/s)</li> <li>• Incidence angle modifier</li> </ul>	<ul style="list-style-type: none"> <li>• 790 (minimum)</li> <li>• 20 (maximum)</li> <li>• <math>2.2 &lt; u &lt; 4.5</math></li> <li>• <math>98\% &lt; \text{normal incidence value} &lt; 102\%</math></li> </ul>

**Table 2:** Physical characteristics

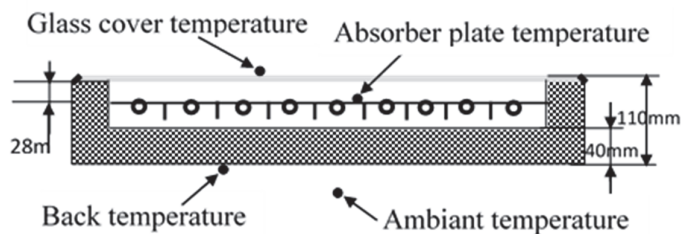
Element collector designation	Dimension (mm)
Riser diameter	12
Header diameter	18
Flat plate collector length	1920
Number of riser tubes	09
Fin height	28



(a) Solar air flat plate solar collector



(b) Solar water flat plate solar collector



(c) Solar water flat plate collector with air absorber cooling

**Figure 1:** Cross-sections of the different configurations



*Solar air flat plate solar collector*



*Solar water flat plate solar collector*



*Solar water flat plate collector with air absorber cooling*

**Figure 2:** Pictures of the solar collectors set up

## 4 RESULTS AND DISCUSSION

Figure 3 shows various parameters used to calculate the heat removal factor according to equation (2.12) and the drawing of the efficiency curves for the different collectors. As it might be noticed, all inlet parameters are practically stable during this measurement period (10h- 15h), which lets us consider the quasi-stationary state. Incident solar radiation is over 800 W/m<sup>2</sup>.

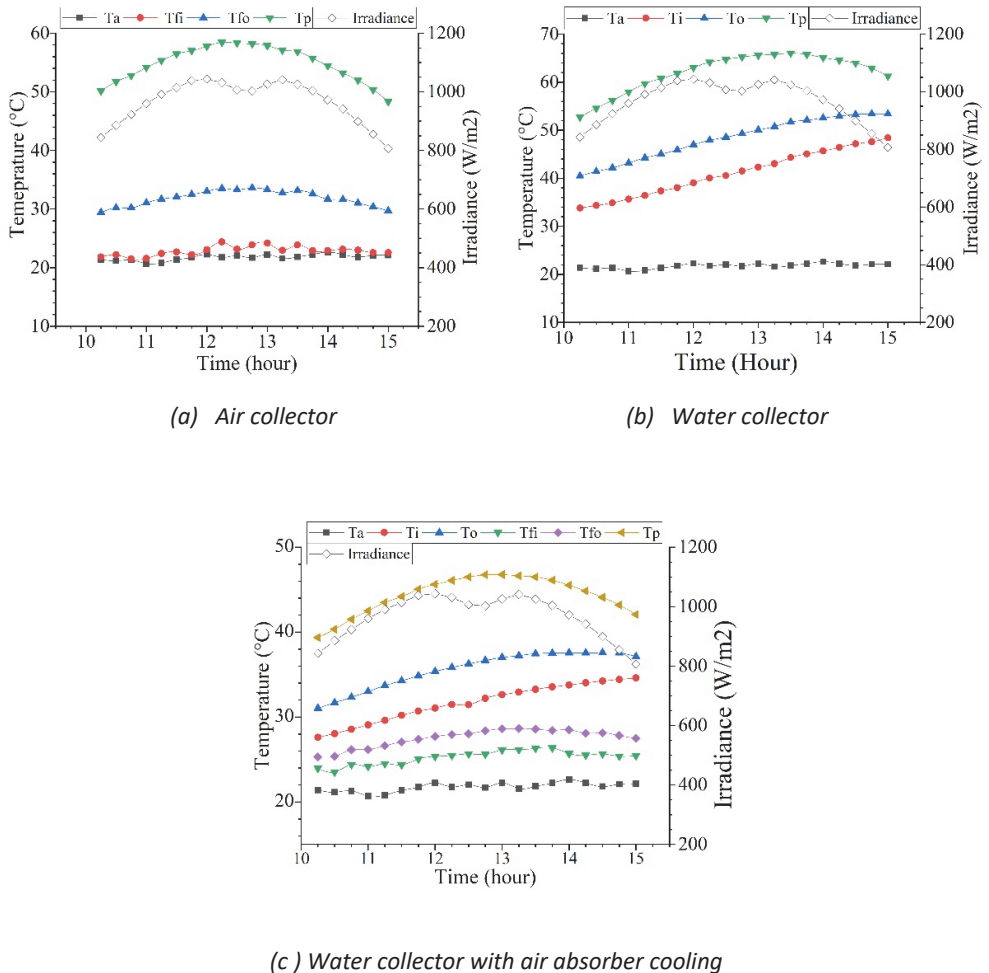


**Figure 3:** Temperatures and solar irradiance for the different configurations

Figure 4 shows the heat removal factors versus the absorber plate temperatures. We observe a small fluctuating value of  $F_R$  around a horizontal line, which might be considered a reference value for this parameter. This indicates that the absorber temperature has a slight influence on  $F_R$ . In contrast, the heat transfer coefficient between the absorber and the fluid flow significantly

impacts  $F_R$ . This confirms that  $F_R$  is an important design parameter as it is a measure of thermal resistance encountered by the absorbed solar radiation in reaching the collector fluid.

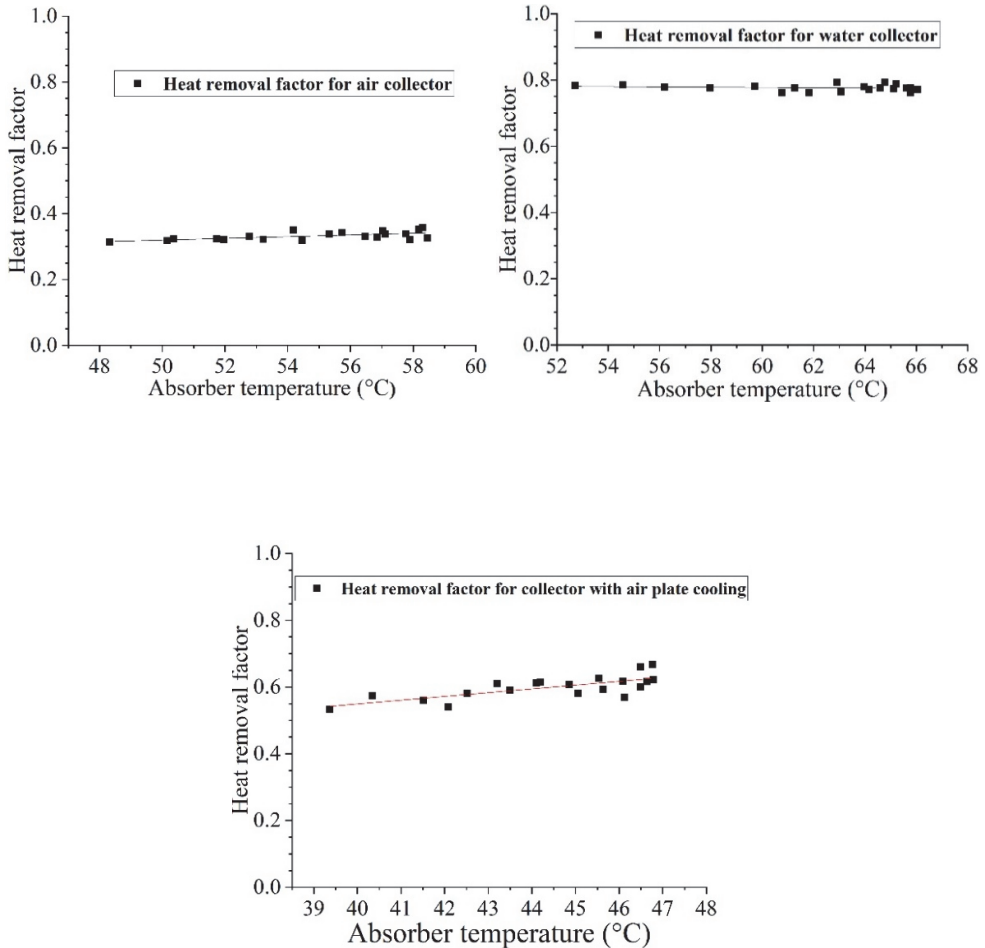


**Figure 4:** Heat removal factor for the different configurations

Figure 5 shows collector efficiencies ( $\eta$ ) versus  $\frac{(T_i - T_a)}{I_g}$ , using experimental data for each configuration. The efficiency coefficient is determined for a mass flow rate of 0.05 kg/s for the air in the solar air collector, 0.11 kg/s for the air in the solar water collector with air absorber cooling, and 0.027 kg/s for water in the solar water collector. The reported values are calculated using experimental data and equation (2.5). It is to recall that, in the case of the configuration of water solar collector with air absorber cooling,  $Q_u$  is the sum of the energy obtained by the flowing water and the energy taken away by the cooling air.

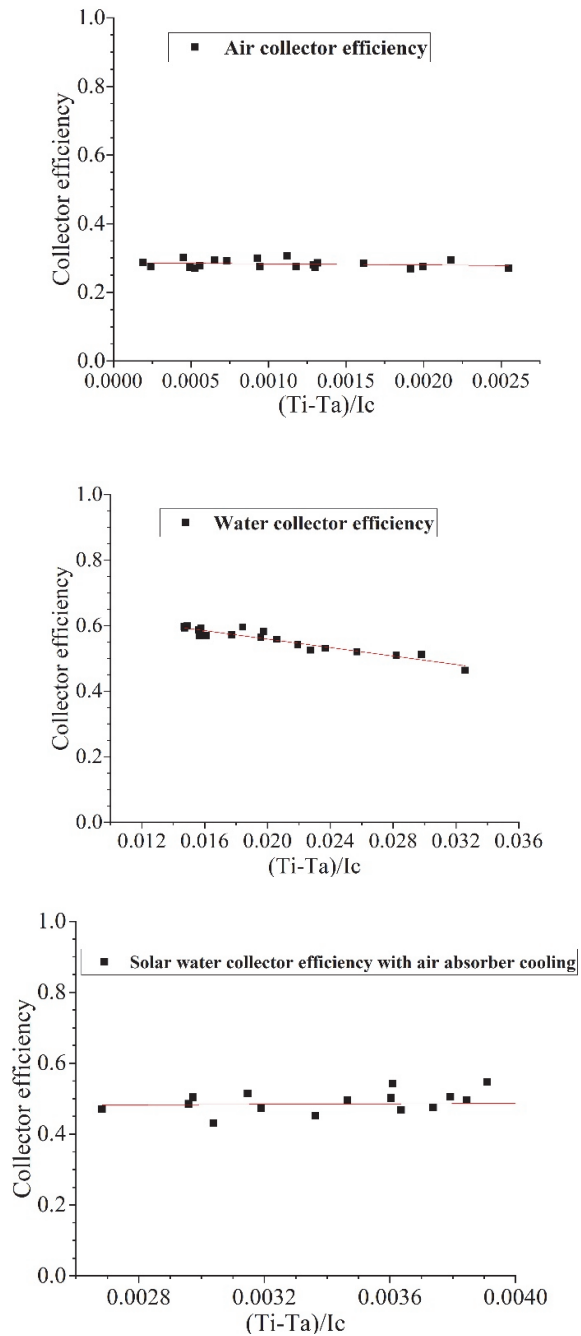


**Figure 5:** Efficiency coefficients for the different configurations

The fitting curve lets us determine the slope. Using the slope and the heat recovery factor calculated with equation (2.12), we can evaluate each collector’s average overall heat loss coefficient. Considering the instantaneous data (efficiency and heat recovery factor), we can also determine the collector’s instantaneous overall heat loss coefficient.

Figures 6, 7, and 8 show the instantaneous overall heat loss coefficients calculated from Klein’s empirical formula and the one deduced experimentally for each configuration versus the absorber temperature. We observe that the overall heat loss deduced experimentally is larger for air collector and water collector. The result is more realistic since it is deduced experimentally. It considers the most influential parameter, which is absorber temperature and all phenomena occurring in the process of heat transmission in any direction. The efficiency coefficient of the solar air collector remains almost constant, regardless of the incident solar flux. This is accompanied by a decrease in the heat loss coefficient. The efficiency coefficient of solar water collector decreases with high irradiance, although there is a decrease in the heat loss coefficient.

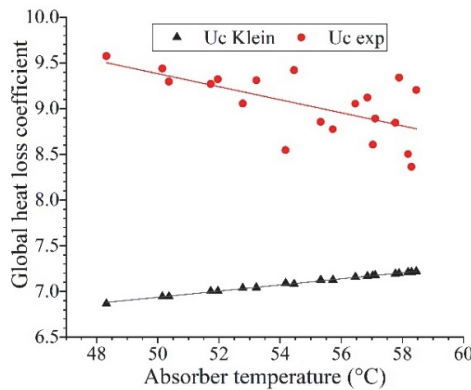


**Figure 6:** Global heat loss coefficient for solar air collector

In the case of a solar water collector with air absorber cooling, the efficiency coefficient is stable at 0.5. The air absorber cooling significantly influences the heat loss coefficient since it decreases with an increase in absorber temperature. In the three cases, the heat loss coefficient calculated with Klein’s empirical formulae increases with absorber temperature increase.

In contrast, the experimental heat loss coefficient decreases for solar air collector and water solar collector with air absorber cooling and uniform for solar water collector with increasing absorber temperature. The average efficiency coefficient of the solar air collector is smaller than the one of the solar water collector with air absorber cooling (Table 3).

**Table 3:** Experimental characteristics for the three solar collector configurations (Uc in W/m<sup>2</sup>.K)

Collector	$\eta$	Slope	$F_R$	Uc_exp	Uc_klein
Air collector	0.283	3.341	0.332	10.063	7.099
Water collector	0.578	6.459	0.776	8.323	7.328
Water collector with air absorber cooling	0.485	3.561	0.599	5.945	6.716

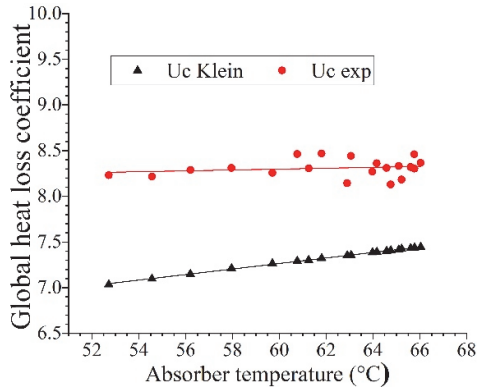


**Figure 7:** Global heat loss coefficient for solar water collector

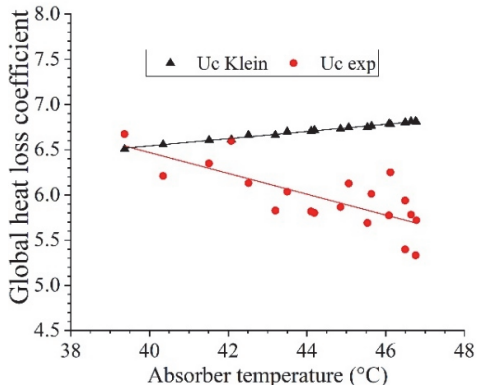


**Figure 8:** Global heat loss coefficient for water collector with absorber back cooling

## 5 CONCLUSION

The evaluation of the thermal loss coefficients is a fundamental task to assess the flat plate solar collector performance, whether in a single solar domestic hot water or a solar collector heat generator or to heat a building or drying system. A new technique for evaluating a global heat loss coefficient of flat plate solar collector was implemented based on experimental data. This technique considers the operating parameters such as temperatures, operating conditions, and geometric characteristics of the collector. The heat removal factor is first deduced using a new formulation based on the most influential parameter: the absorber temperature. From the slope of the efficiency coefficient fitting line, the global heat loss coefficient is determined. The result analysis and the comparison with thermal loss coefficients obtained from Klein’s empirical formula indicate that this technique generates a more realistic value for the global heat loss coefficient. The coefficient deduced with this procedure will let the designer and the solar system developer be more confident in determining the dimensions and the expected power. The rapid determination of  $F_R$ , which is an important design parameter, lets the developer appreciate thermal resistance encountered by the absorbed solar radiation in reaching the collector fluid. A

precise knowledge of the characteristic of the collector lets the designer correctly establish the dimensions of any solar heating system.

## References

- [1] **W. Weiss, M. Spörk-Dür:** *Solar Heat Worldwide. Global Market and trends in 2019*, AEE – Institute for sustainable Technologies, Gleisdorf Austria, 2020
- [2] **A. Saxena, Varun, A.A. El-Sebaii:** *A thermodynamic review of solar air heaters*, *Renew. & Sustain. Energy Rev.*, Vol.43, pp.863–890, 2015
- [3] **A.L. Hernandez, J.E. Quinonez:** *Experimental validation of an analytical model for performance estimation of natural convection solar air heating collectors*, *Renew. Energy*, Vol. 117, pp.202–216, 2017
- [4] **F. Chabane, N. Moummia, S. Benramache:** *Experimental analysis on thermal performance of a solar air collector with longitudinal fins in a region of Biskra, Algeria*, *Journal of Power Technologies*, Vol.93 iss.1, pp.2013, 52–58. 2013
- [5] **S.A. Sakhaei, M.S. Valipour:** *Performance enhancement analysis of the flat plate collectors: a comprehensive review*, *Renew. Sustain. Energy Rev.*, Vol. 102, pp.186–204, 2019a
- [6] **S.A. Sakhaei, M.S. Valipour:** *Investigation on the effect of different coated absorber plates on the thermal efficiency of the flat-plate solar collector*, *J. Therm. Anal. Calorim*, Vol.140 Iss.3, pp.1-14, 2019b
- [7] **A. Jamar, Z.A.A. Majid, W.H. Azmi, M. Norhafana, A.A. Razak:** *A review of water heating system for solar energy applications*, *International Communications in Heat and Mass Transfer*, Vol. 76, pp.178–187, 2016
- [8] **K.M. Pandey, R. Chaurasiya:** *A review on analysis and development of solar flat plate collector*, *Renew. Sustain. Energy Rev.*, Vol. 67, pp.641–650, 2017
- [9] **Z. Pluta:** *Evacuated tubular or classical flat plate solar collectors*, *Journal of Power Technologies*, Vol. 91 ISS.3, pp.158–164, 2011
- [10] **D. Alta, E. Bilgili, C. Ertekin, O. Yaldiz:** *Experimental investigation of three different solar air heaters: Energy and exergy analyses*, *Appl. Energy* Vol. 87, pp.2953-2973, 2010
- [11] **M. Hamed, A. Fella, A. BenBrahim:** *Parametric sensitivity studies on the performance of a flat plate solar collector in transient behavior*, *Energy Conversion and Management*, Vol. 78, pp.938-947, 2010
- [12] **S.A. Klein:** *Calculation of flat-plate collector loss coefficients*, *Solar Energy*, Vol. 17 iss.1, pp.79–80, 1975
- [13] **R. Bliss:** *The derivations of several “Plate-efficiency factors” useful in the design of flat-plate solar heat collectors*, *Solar Energy*, Vol.3, pp.55-64, 2009
- [14] **A. Whillier:** *Performance of Black Painted Solar Heaters of Conventional Design*, *Solar Energy*, Vol. 8, pp.31-37, 1964
- [15] **M. Esen:** *Thermal performance of a solar cooker integrated vacuum-tube collector with heat pipes containing different refrigerants*, *Solar Energy*, Vol. 76, pp.751–757, 2004

- [16] **H. Esen, M. Esen, O. Ozsolak:** *Modelling and experimental performance analysis of solar-assisted ground source heat pump system*, J. Exp. Theoret. Artif. Intell., Vol. 29, pp.1–17, 2017
- [17] **S. Kalogirou:** *Solar energy engineering: processes and systems* - 1st ed. p. cm. Elsevier Academic Press. 2009, ISBN 978-0-12-374501-9, 2009
- [18] **ANSI/ASHRAE Standard 93-2003:** *Methods of Testing to Determine the Thermal Performance of Solar Collectors*, ASHRAE, Inc.; 2003

## Nomenclature

$A_c$	Total collector aperture area (m <sup>2</sup> )
$h_{c,b-a}$	Convection heat loss coefficient from back to ambient (W/m <sup>2</sup> .K)
$h_{c,e-a}$	Convection heat loss coefficient from edge to ambient (W/m <sup>2</sup> .K)
$h_w$	Wind heat transfer coefficient (W/m <sup>2</sup> .K)
$I_c$	Irradiance on the collector (W/m <sup>2</sup> )
$k_b$	Conductivity coefficient of back insulation (W/m.K)
$k_e$	Conductivity coefficient of edge insulation (W/m.K)
$L$	Collector length (m)
$\dot{m}$	Mass flow rate of fluid (kg/s)
$N_g$	Number of glass covers
$Q_u$	Rate of useful energy delivered by the collector (W)
$T_a$	Average ambient temperature (°C)
$t_b$	Thickness of back insulation (m)
$t_e$	Thickness of edge insulation (m)
$T_{fi}$	Air collector inlet temperature (°C)
$T_{fo}$	Air collector outlet temperature (°C)
$T_i$	Water collector inlet temperature (°C)
$T_o$	Water collector outlet temperature (°C)
$T_p$	Average temperature of the absorbing surface (°C)
$U_b$	Bottom heat loss coefficient (W/m <sup>2</sup> .K)
$U_e$	Edges heat loss coefficient (W/m <sup>2</sup> .K)
$U_c$	Solar collector overall heat loss coefficient (W/m <sup>2</sup> .K)
$U_t$	Top heat loss coefficient (W/m <sup>2</sup> .K)
$V$	Wind velocity (m/s)



# TOWARDS FORTY YEARS OF KRŠKO NPP OPERATION – AN OVERVIEW OF POPULATION EXPOSURES TO RADIATION

## OB KONCU ČETRTEGA DESETLETJA DELOVANJA NE KRŠKO - PREGLED SEVALNE IZPOSTAVLJENOSTI PREBIVALSTVA

Matjaž Koželj<sup>✉</sup>

**Keywords:** Krško NPP, NEK, radioactivity monitoring, radioactivity releases, dose assessment, population exposures, history of doses.

### **Abstract**

In this article, the influence of a controlled magnetic field on gadolinium plates was modelled and simulated to be used in magnetic refrigeration installations. This is a state-of-the-art technology that does not use refrigerants and does not work based on vapour compression, which is based on the operation of the magnetocaloric properties of the material used; in the case below, this material, in the form of a flat plate, has certain magnetocaloric properties and under the influence of magnetic induction can be used successfully in such innovative installations. The advantages of using gadolinium in the form of a flat plate in a magnetic regenerator and thermal energy dissipation on its surface under the controlled magnetic field's influence were studied.

### **Povzetek**

V prispevku so predstavljene omejitve za radioaktivne izpuste iz Nuklearne elektrarne Krško, ki so z manjšimi spremembami v veljavi od začetka delovanja. Monitoring, ki se izvaja v okolici elektrarne,

<sup>✉</sup> Corresponding author: mag. Matjaž Koželj, Jožef Stefan Institute, Milan Čopič Nuclear Training centre, Jamova 39, 1000 Ljubljana, Slovenia, Tel.: +386 1 588 5277, E-mail address: [matjaz.kozelj@ijs.si](mailto:matjaz.kozelj@ijs.si)

se ni bistveno spremenil od poznih osemdesetih let. Predstavljeni so zbrani podatki o radioaktivnosti v tekočinskih in atmosferskih izpustih. Zbrani podatki o ocenjenih dozah kažejo, da so skozi leta bili v uporabi različni pristopi ocenjevanju doz, vendar vsi dokazujejo, da so doze prebivalstva bile vedno bistveno manjše od avtoriziranih mejnih doz.

## 1 INTRODUCTION

The construction of the Krško Nuclear Power Plant (Krško NPP, NEK) started in 1975 and was concluded in 1981. The first criticality took place in September 1981, and the first synchronization with the grid occurred in October 1981. In 1982, numerous tests were performed and, finally, in January 1983, NEK started commercial operation. One year later (in January 1984), the regular operation of NEK was approved.

The introduction of nuclear energy was a great challenge for involved scientific and technical experts, legislators, and all domestic companies acting either as contractors or subcontractors during the construction and later, supporting the operation and maintenance of NEK. Besides nuclear safety, one of the most important challenges was how to define legal restrictions regarding the radiation influence of NEK on the population and environment and how to establish proper control mechanisms to ensure and verify that the restrictions are followed. Although in the former Yugoslavia adopting relevant legislation and rules regarding nuclear and radiation safety took almost a decade, the very basic requirements for the safe operation of NEK were established and were set early, before the start of the operation. Later, the requirements were additionally elaborated, but, as we will see, the original restrictions have not been altered.

## 2 LEGAL RESTRICTIONS

The first limit for the radiation impact of NEK on the environment was established ten years before the official start of regular operation in the Location Permit issued by the National Secretariat for Urbanism of Slovenia in 1974. The Location Permit required that the (effective) dose<sup>i</sup> from the radioactive releases of NEK on the border of the restricted protective zone (500 m from the reactor axis) and beyond shall not exceed 50  $\mu\text{Sv}$  per year. The Location Permit also required that reference (pre-operational) measurements be performed and possible consequences of NEK operation (radioactivity releases and distribution) on the surface and underground waters in Krško and Zagreb basins estimated and assessed. Due to the lack of national regulations regarding the use of nuclear energy at that time, relevant regulations from the country of origin of installed equipment (i.e., the USA), or applicable recommendations from the International Atomic Energy Agency should be used in cases in which appropriate national regulations were insufficient or non-existent. It was optimistically foreseen that the investors (i.e.,

---

<sup>i</sup> *Effective dose* is a quantity used to describe the consequences of exposure of human being to ionising radiation and considers external and internal exposure. It is used for low doses and represents the measure of probability for the occurrence of radiation-induced cancer and genetic effects. The unit for effective dose is the sievert (Sv). For reference, the global annual average is 2.4 mSv.

Slovenia and Croatia) would find the solution and decide on the location of the final repository for all future radioactive waste from NEK before commissioning the plant.

The limit for the effective dose established in the Location Permit has never been changed and remains valid. In 1988, an additional requirement was added in connection with the construction of temporary storage for Low and Intermediate Level Radioactive Waste. According to this requirement, the annual effective dose from external radiation at the NEK fence shall not exceed 200  $\mu\text{Sv}$ . The storage is still in operation.

During the construction period of NEK, rules were adopted related to monitoring and limits of contamination in the environment and exposure limits for the population from different practices. In the decision regarding the approval of regular operation of NEK (February 1984), additional restrictions regarding liquid effluents from NEK to the Sava River were set:

- For all radionuclides except  $^3\text{H}$  (Tritium),  $^{14}\text{C}$  and dissolved gases: 200 GBq per year and 80 GBq in a calendar quarter,
- For  $^3\text{H}$ : 20 TBq per year, 8 TBq in a calendar quarter.

Annual limits for activity releases in gaseous releases were not set explicitly in the decision. Instead, NEK was required to provide computational models for the dilution of releases during normal operation and the dispersion of releases during the potential accident that could serve as a basis for the dose calculation to the public. In response to this requirement, NEK has developed models based on the recommendations from the US Nuclear Regulatory Commission that were used for establishing the annual limits for activities in gaseous releases from NEK. The annual limits for activities in gaseous releases were officially confirmed in 1989 and were as follows:

- For  $^{131}\text{I}$  (Iodine): 18.5 GBq per year,
- For aerosols (radionuclides with  $T_{1/2} > 8$  d): 18.5 GBq per year,
- For noble gases: the annual limit is calculated from the dose limit (50  $\mu\text{Sv}$  per year) on the border of the restricted protective zone according to adopted models,
- For  $^3\text{H}$  and  $^{14}\text{C}$  there were no explicit limits for released activities.

These limits were in force until 2007, when the limits for liquid effluents were modified to allow for a longer (18 months, previously 12 months) fuel cycle in NEK. The annual limit for the  $^3\text{H}$  release was increased, while the limit for other liquid releases was decreased. The new (and still valid) limits for liquid effluents are:

- For all radionuclides except  $^3\text{H}$ ,  $^{14}\text{C}$  and dissolved gases: 100 GBq per year, 40 GBq in a calendar quarter,
- For  $^3\text{H}$ : 45 TBq per year,
- For  $^{14}\text{C}$ : no explicit limit.

Since 2007, the limits for gaseous releases and liquid effluents are a part of the Radiological Effluent Technical Specifications (RETS), a document related to radiological safety, monitoring, effluents, and reporting requirements. This document must be approved by a regulatory body for a valid operating licence and must be continuously maintained to reflect possible modifications and compliance with legal requirements.

We can see that “the history” of dose and radioactive release limits for NEK is quite short and, except for the adjustment related to the introduction of 18-month fuel cycle, there has been no change of limits from the beginning of NEK operation. The reason is not in the indifference and

passivity of the authorities but the professional knowledge of involved experts and adoption of internationally approved approach during the initial licensing process and initial operation of the plant.

The author aims to review available data on emissions from NEK and compare it with available data on doses of the population in the NEK neighbourhood. We made such a comparison ten years ago, [1], and we would like to update data and verify conclusions from the previous paper.

### 3 MONITORING

The NEK must provide proof that it is complying with the imposed restrictions. Therefore, it is obliged to measure the emissions of radionuclides and report them to the regulatory body, and also to provide an independent assessment of effects to the environment and population. Monitoring, therefore, consists of the measurements of the plant releases (a measurement of emissions), sampling, and measurements in the plant neighbourhood (a measurement of immissions in the environment), evaluation of these measurements, as well as total dose assessment for members of the public based on collected data and/or computational models. Objectiveness and validity of results have been ascertained with the involvement of independent and authorised organizations (experts) in the monitoring implementation, evaluation of data and dose assessment.

Requirements for monitoring in environment and emissions reporting have been in force from the very beginning of the operation of NEK. The programme of sampling and measurements, which has been verified and approved annually, has been based on a generic (and extensive) programme in the relevant rules from 1986 and the rules from 2007. The main difference between these rules is not in the content of the monitoring programme itself but the introduction of the additional requirements related to the quality and reliability of measurements. The rules were updated in 2018 when Council Directive 2013/59/Euratom was adopted in Slovenian legislation.

Monitoring in the environment covers a 12 km circle around the plant and extends 30 km downstream of the River Sava. It includes:

- external dose measurements with passive and active detectors,
- sampling and measurement of radioactivity in the air (aerosols and iodine),
- sampling and measurement of radioactivity in the river Sava (water, sediments, fish),
- sampling and measurement of soil,
- sampling and measurement of drinking water (wells and water supplies),
- sampling and measurement of atmospheric precipitations and deposits,
- sampling and measurement of food and milk (locally produced).

In Figure 1, sampling locations for monitoring are presented (from [2]). Comparison of this figure with the figure from the report, [3], from 1991 reveals that the number of sampling points has not changed substantially from the late 1980s, and that sampling positions are not changed for the majority of "old" locations.

In addition to sampling, monitoring also includes external dose measurements with passive TL detectors and continuous active detectors (energy compensated GM tubes) for external dose rate measurements. While the active detectors are a part of the early warning system in Slovenia and

were not operational until the late 1990s, the network of TL detectors around NEK (57 locations, up to 10 km from the plant) has just slightly been changed from the 1990s.

In support of monitoring and emergency preparedness, one meteorological station is situated inside the plant and three in the vicinity of the plant. The data from these stations serve for computational modelling required in dose assessment.

All data from monitoring are collected and evaluated through authorised organizations on a regular basis. Evaluated data from environment monitoring and data on NEK emissions are used for the dose assessment of members of the public in the neighbourhood of NEK. Evaluated monitoring data, as well as results of dose assessment, are published on an annual basis as a report, which is also publicly available through the NEK internet site.

Data from continuous detectors in the early warning system from all parts of Slovenia are publicly available on the internet, [4].

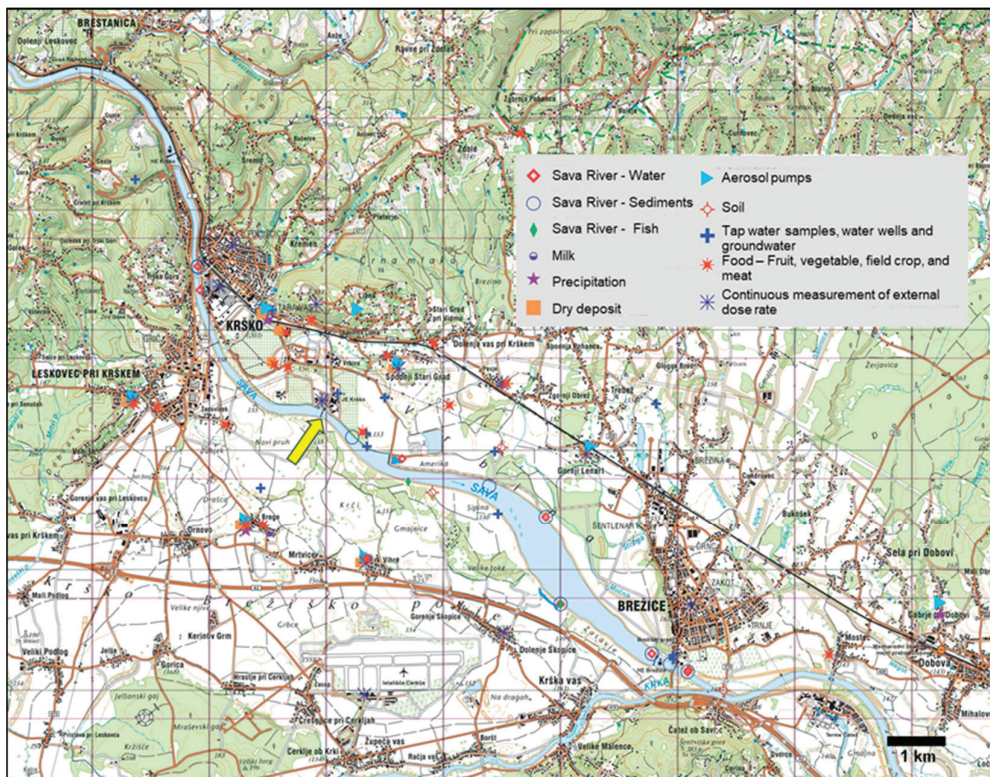


**Figure 1:** Current map of NEK neighbourhood with the distribution of places where different samples are regularly taken as a part of NEK monitoring, [2]. The position of NEK is marked with an arrow.

## 4 OVERVIEW OF EMISSIONS FROM NEK

As stated, for the purpose of monitoring, NEK provides data on released activities in all liquid effluents and gaseous releases from the beginning of operation (first criticality). All releases are continuously measured and data are collected. Released activity depends on many factors, but the most important factors are fuel quality, leaks from the primary system, produced power, trips and power excursions, the efficiency of liquid and gaseous waste processing, the chemistry of the primary system, and also an implementation of outages, and remediation of possible equipment failures.

### 4.1 Liquid effluents

The history of annual activity releases in liquid effluents of NEK from 1983 to 2019 (data from [5]) is presented in Figure 2. We can see that the annual releases of fission and activation products (Figure 2a) have been steadily decreasing since the first years of operation. However, even the highest value (13.4 GBq in 1985) was a mere 6.7% of the annual limit (200 GBq per year until 2007). The values in 2008 and 2009 (the last one not presented in the figure) were under 100 MBq (less than 0.1% of the valid annual limit 100 GBq per year). The main contributors to annual releases were (and still are) activation products such as  $^{58}\text{Co}$  and  $^{60}\text{Co}$  (Figure 2c), and fission products  $^{134}\text{Cs}$  and  $^{137}\text{Cs}$  (Figure 2d). The released activity of  $^{131}\text{I}$  (Figure 2b) was always at least ten times lower and, in the last two decades, appears in the liquid effluents only occasionally.

While the annual released activity of almost all radionuclides in liquid effluents has decreased substantially since the beginning of the operation, this does not apply to  $^3\text{H}$  (Figure 2e). The reason is in a direct connection between  $^3\text{H}$  production and energy production in NEK. The released activity was always close (40% to 80%) to the valid limit (20 TBq until 2007). In connection with the introduction of the 18-month fuel cycle, the Slovenian Nuclear Safety Administration has changed the limit to 45 TBq.

### 4.2 Gaseous releases

The history of annually released activities in gaseous releases of NEK from 1983 to 2019 (data from [5]) is presented in Figure 3. The most important radionuclides are noble gases ( $^{133}\text{Xe}$ ,  $^{133\text{m}}\text{Xe}$ ,  $^{41}\text{Ar}$ ), which are limited indirectly through effective dose on the NEK fence, and  $^3\text{H}$  (no limit). The highest releases of noble gases (Figure 3a) were in the mid-1990s (up to 25 TBq), while the current values are around 1 TBq.

Similarly as in liquid effluents, an annual release of  $^3\text{H}$  in gaseous releases does not show any decrease (Figure 3b). After the introduction of an 18-month fuel cycle, the annually released activity is around 2.5 TBq. History of releases of  $^{14}\text{C}$  (Figure 3c), in contrast, shows an initial decrease from the first value of 400 GBq (1985) in the 1980s but has not substantially changed in the last two decades. The annual release is around 100 GBq.

Annual releases of  $^{131}\text{I}$  (not presented in Figure 3) have been under 1 MBq since 2001. In the 1990s, these values were much higher, up to 2.7 GBq in 1996, which is 15% of the limiting value (18.5 GBq per year). In 1996, to our knowledge, was also the highest release activity of aerosols (20 MBq, 0.1% of limiting value). Annual activity releases of aerosols in the last decade are about MBq or less.

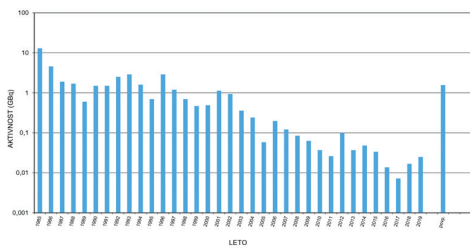


Figure 2a: Fission and activation products. The annual limit (200 GBq) was changed to 100 GBq 2007.

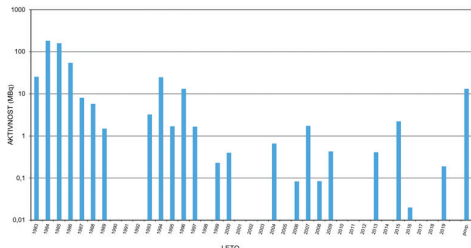


Figure 2b: Iodine ( $^{131}\text{I}$  equivalent). The release is limited by the total limit for fission and activation products.

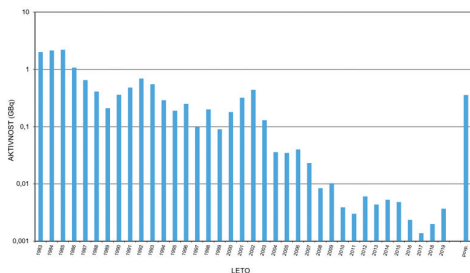


Figure 2c: Cobalt ( $^{60}\text{Co}$  equivalent). The is limited by the total limit for fission and activation products.

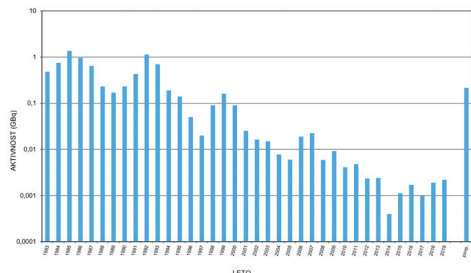


Figure 2d: Caesium ( $^{137}\text{Cs}$  equivalent). The release is limited by the total limit for fission and activation products.

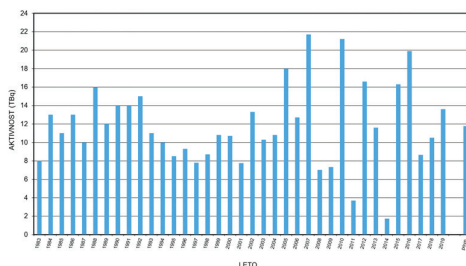


Figure 2e:  $^3\text{H}$  (Tritium). The annual limit (20 GBq) was changed to 45 GBq in 2007.

Figure 2: Annual activity releases in liquid effluents of NEK for 1983-2019 (from [5]).

Annual releases of  $^{14}\text{C}$  are presented in Figure 3c. Releases were much higher in the 1980s than in the 1990s and later, when annual gaseous releases were 0.1 TBq per year or less. An annual limit has not been established for this radionuclide (the same also applies to other nuclear power plants) and the impact on population doses was not properly evaluated until 2002.

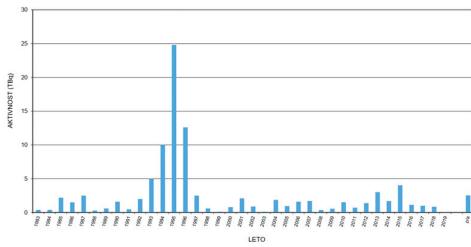


Figure 3a: Noble Gases. The release is limited indirectly through a limited effective dose ( $50 \mu\text{Sv}$  per year) on the border of the restricted area.

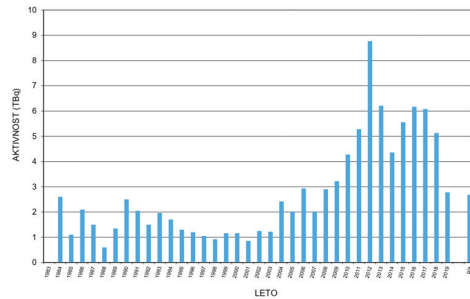


Figure 3b:  $^3\text{H}$  (Tritium). The annual limit has not been established.

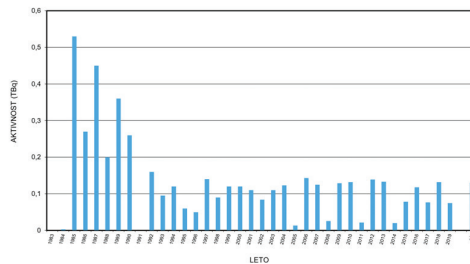


Figure 3c:  $^{14}\text{C}$ . The annual limit has not been established.

Figure 3: Annual activity releases in gaseous releases of NEK from 1983 to 2019 (from [5]).

## 5 COMPARISON OF ASSESSED DOSES

Data from the monitoring of emissions from NEK and immissions of radionuclides into the environment serve as a starting point for the evaluation of doses to the general population in the neighbourhood of NEK. This assessment is done by authorised organisations and finally submitted to the regulatory body through NEK. We will not discuss in detail methods or methodology of dose assessment in the past but merely present the data compiled from the available report on the evaluation of the radiological monitoring of the Krško Nuclear Power Plant in the 1980s, [3], and available national annual reports on the radiation and nuclear safety in the Republic of Slovenia, [6].

### 5.1 Doses from liquid releases

In Figure 4, doses from NEK liquid releases are presented with total doses from all releases (including gaseous). We can see that until 1994 almost all dose from NEK was associated with liquid releases. It was related to local fishermen and their families, and the most important radionuclide for this exposure pathway is  $^{137}\text{Cs}$ .

However, we must point out that the total dose is not always a realistic term. It is not always possible to simply add doses from different exposure pathways since the complete dose assessment includes dose estimates for different and distinct critical groups of people. Comparison with data on Figure 2 can therefore hardly support the observable increase of annual doses in the first half of the 1990s in Figure 4.

Doses from liquid releases were practically constant through the second half of the 1990s and diminished for almost an order of magnitude in 2002, which also applies to the total dose from NEK. Both changes were the consequence of the changed methodology for dose assessment.

If we consider the last decade, the contribution of  $^{14}\text{C}$  to doses from liquid releases and to total doses was prevailing from 2013 to 2016 but became minimal in 2017.

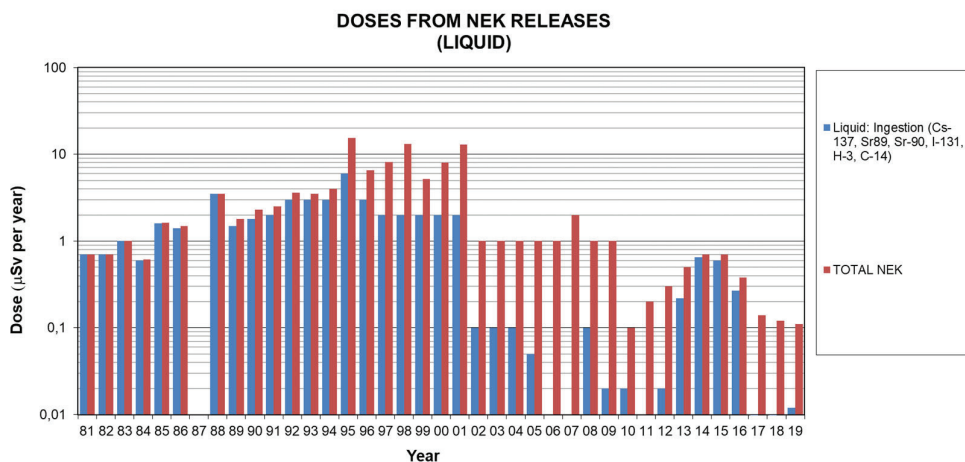


**Figure 4:** Annual doses of the population in the NEK neighbourhood due to liquid releases ([3], [6]).

## 5.2 Doses from gaseous releases

Available data on annual doses from gaseous releases from NEK are presented in Figure 5. After 1994 (and until 2001), the most important exposure pathway was external exposure from the cloud of noble gases. Data in Figure 3a reveals that the release of noble gases was high in 1993 to 1996, but not in 1997 and afterward. However, assessed doses from noble gases were high until 2001.

After 2001, the most important pathway was the ingestion of radionuclides from gaseous releases transferred to vegetation. The most important radionuclide in this respect is  $^{14}\text{C}$ , which becomes a part of the food chain.  $^{14}\text{C}$  was not included in the evaluation before 2002, and its contribution was not regularly measured until the last decade. Contribution to the dose in 2002 (and in the following years) was estimated based on analogous results with other nuclear power plants. This was also the consequence of the methodology change mentioned in the discussion

of the doses from liquid releases. In this period, the inhalation dose from  $^3\text{H}$  was comparable to the estimated dose from  $^{14}\text{C}$ .

In the previous decade, the doses from gaseous releases were related mostly to  $^{14}\text{C}$ . These doses were assessed from measurements in the environment and could be considered realistic values for the NEK neighbourhood.

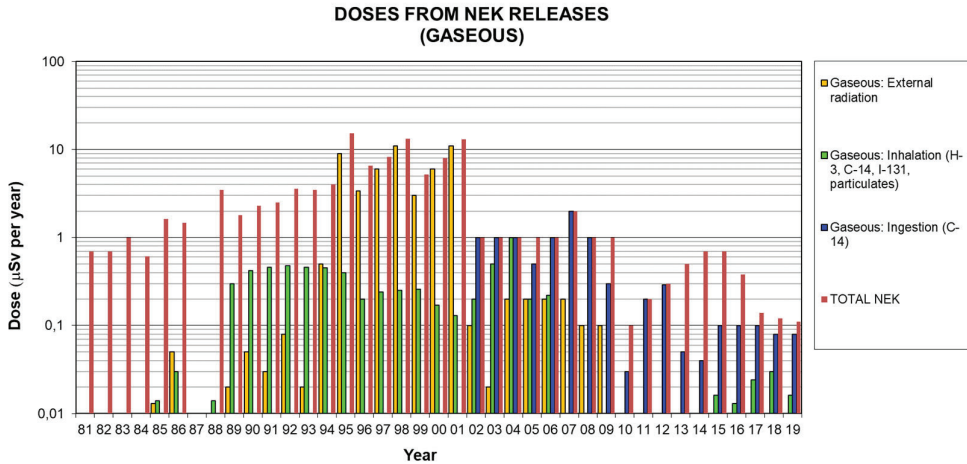


**Figure 5:** Annual doses of the population in the NEK neighbourhood due to gaseous releases ([3], [6]).

### 5.3 Importance of pathways

In Figure 6, doses from liquid and gaseous releases are presented together with estimated total doses from NEK releases. The scale in the figure is linear to enable easier comparison of release pathway importance through the period from 1981 to 2019.

In Figure 6, we can see that until 1994, total annual doses were approximately 2 to 4  $\mu\text{Sv}$  per year. The most important contribution was the ingestion dose due to liquid effluents. From 1995 to 2001, total doses were from 5 to 15  $\mu\text{Sv}$  per year, but the most important contribution comes from external exposure to gaseous releases (up to 11  $\mu\text{Sv}$  per year). This was the external exposure to radiation from a cloud of noble gases released from the plant. The assessed ingestion dose due to liquid releases was still high (2 to 6  $\mu\text{Sv}$  per year).

From 2002 to 2019, total doses are (less than) 1 to (less than) 2  $\mu\text{Sv}$  per year. The most important contribution is the ingestion dose due to the release of  $^{14}\text{C}$ . The estimate considers the transfer of  $^{14}\text{C}$  from air to local vegetation and food chain and  $^{14}\text{C}$  in liquid releases which is consumed by local fishermen. All other pathways contribute much lower doses.

We can also see that estimated doses have never come close to the authorised limit. Even the highest estimated dose (from 1995) represents only 30% of the authorised limit.

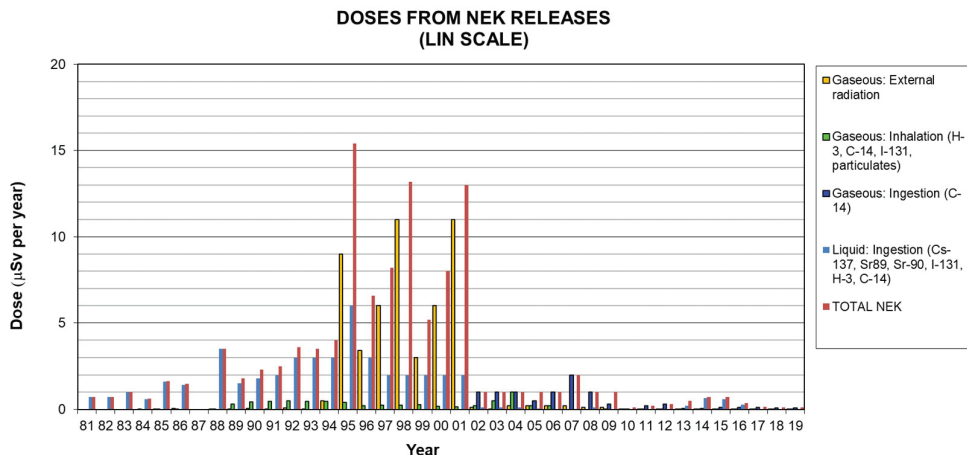


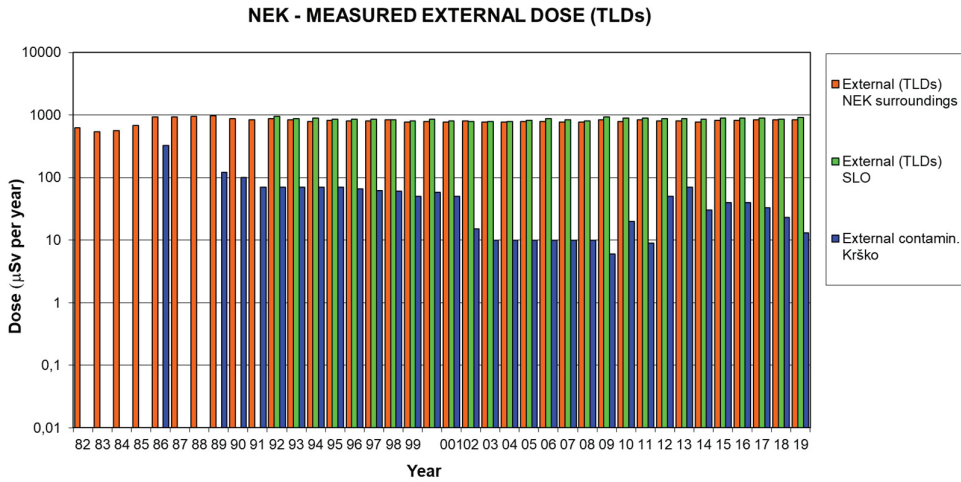
**Figure 6:** Annual doses of the population in the NEK neighbourhood due to all releases ([3], [6]). The scale is linear to enable easier comparison of release pathways importance.

## 5.4 Comparison with natural background and global contamination

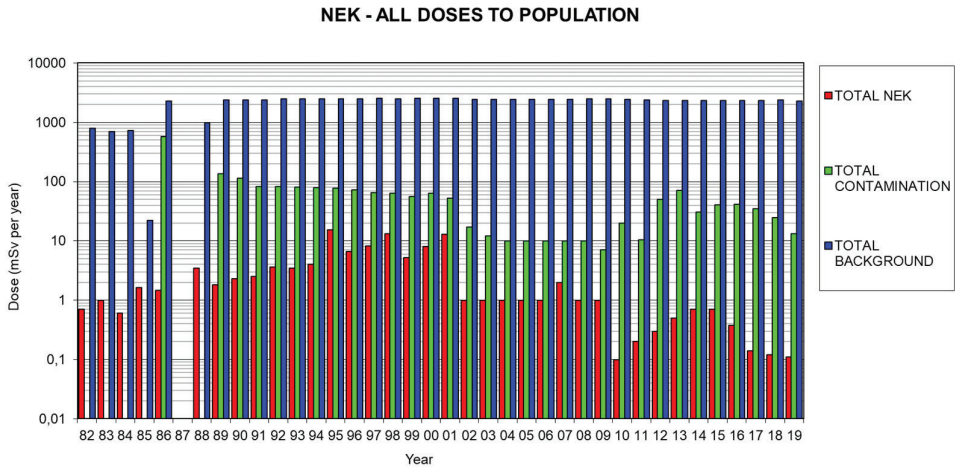
Measurements of radioactivity in the neighbourhood of NEK provide us also with the data that enable us to assess natural radiation background. Similar data are available also for Ljubljana and other parts of Slovenia.

Figure 7 presents annual external exposures to radiation measured with the TLDs in the neighbourhood of NEK, average external exposures in Slovenia (also measured with TLDs) and estimated annual external doses due to contamination from nuclear tests and Chernobyl releases in the NEK neighbourhood. The highest contribution of contamination to external dose was in 1986 (after Chernobyl) when the annual external dose from contamination was estimated to 325  $\mu\text{Sv}$ . We can see that the annual external dose, as measured with the TLDs in the NEK neighbourhood, was regularly slightly below the Slovenian average. We can also see that the contribution of external radiation to dose was significant only in the 1980s.

In Figure 8, the total annual doses to the population in the NEK neighbourhood from NEK operation are compared to total doses from natural sources (natural background) and total doses due to contamination from nuclear tests and Chernobyl releases. We can see that measured natural background (2440 to 2530  $\mu\text{Sv}$  per year, which is practically the same as measured in Ljubljana) was always the main contributor to the total dose of population. In 1986, when the Chernobyl accident happened, the contribution of total contamination was 570  $\mu\text{Sv}$  (in Ljubljana even 720  $\mu\text{Sv}$ !), while is the estimated current value is about 10  $\mu\text{Sv}$  per year. The highest estimated annual dose from NEK (15.4  $\mu\text{Sv}$  in 1995) was 31% of the administrative dose limit and only 0.6% of natural background, while the (overestimated) annual doses from recent years (less than 0.15  $\mu\text{Sv}$ ) present only 0.3% of administrative dose limit and 0.006% of natural background.



**Figure 7:** Comparison of average annual external doses measured in the neighbourhood of NEK (57 TLDs), average external doses measured in Slovenia to annual external doses contamination estimated from measurements of soil contamination in NEK neighbourhood ([3], [6]).



**Figure 8:** Comparison of annual doses of the population in the neighbourhood of NEK from exposure to natural sources, general contamination from nuclear tests and Chernobyl releases, and nuclear power plant.

## 6 CONCLUSIONS

We have seen that initial limitations imposed on the operation of NEK remain valid and, except in the case of liquid discharge of  $^3\text{H}$ , there was no need to modify them.

NEK successfully operates within these limitations with releases, which are well below the limiting values.

The scope and extent of monitoring have not changed substantially from the mid-1980s; therefore, old data remain compatible with recent measurements.

We can recognise different approaches to dose evaluation in certain periods of monitoring history. Therefore, doses from different periods are not always directly comparable.

According to the available data, except in the late 1990s, estimated doses to the population were always only a few percent points of the authorised dose limit, which is 50  $\mu\text{Sv}$  per year.

## References

- [1] **M. Koželj:** *A brief history of Krško NPP radiation impact on environment*, Proceedings of the International Conference Nuclear Energy for New Europe 2010, Portorož, Slovenia, September 6-9, 2010
- [2] **Nuklearna Elektrarna Krško:** *Meritve emisij in radioaktivnosti v okolju, Zemljevid merilnih mest* [online]. Available: <https://www.nek.si/sl/okolje/meritve-emisij-in-radioaktivnosti-v-okolju> (10 February 2021)
- [3] **B. Breznik, A. Kovač:** *Poročilo desetletnega obdobja radiološkega nadzora v okolici Nuklearne elektrarne Krško*, Nuklearna elektrarna Krško, Krško, 1991
- [4] **Uprava Republike Slovenije za jedrsko varnost:** *Mreža zgodnjega opozarjanja, Trenutne vrednosti sevanja gama v okolju* [online], Radioaktivnost v okolju. Available: [https://radioaktivnost.si/rvo\\_public/RVO/Map](https://radioaktivnost.si/rvo_public/RVO/Map) (15. February 2021)
- [5] **Uprava Republike Slovenije za jedrsko varnost:** *Razširjeno poročilo o varstvu pred ionizirajočimi sevanji in jedrski varnosti v Republiki Sloveniji leta 2019*, URSJV/DP-216/2020, Ed. Benja Režonja, Uprava RS za jedrsko varnost, 1920
- [6] **Uprava Republike Slovenije za jedrsko varnost:** *Annual Reports on Radiation Protection and Nuclear Safety in Slovenia* [online], 1992-2020. Available: <https://www.gov.si/drzavni-organi/organi-v-sestavi/uprava-za-varstvo-pred-sevanji/o-upravi-republike-slovenije-za-varstvo-pred-sevanji/letna-porocila-o-varstvu-pred-ionizirajocimi-sevanji-in-jedrski-varnosti-v-republiki-sloveniji/> (10 February 2021)



# COMPARISON OF CAVITATION MODELS FOR THE PREDICTION OF CAVITATION AROUND A HYDROFOIL

## PRIMERJAVA KAVITACIJSKIH MODELOV ZA NUMERIČNO NAPOVED KAVITACIJE NA HIDRODINAMIČNEM PROFILU

Marko Pezdevšek<sup>33</sup>, Ignacijo Biluš, Gorazd Hren

**Keywords:** Hydrofoil, cavitation, Ansys CFX

### **Abstract**

In this paper, four different cavitation models were compared for predicting cavitation around a hydrofoil. A blocked structured mesh was created in ICEM CFD. Steady-state 2D simulations were performed in Ansys CFX. For all cases, the SST turbulence model with Reboud's correction was used. For Zwart and Schnerr cavitation models, the recommended values were used for the empirical coefficients. For the full cavitation model and Kunz cavitation model, values for the empirical coefficients were determined as the recommended values did not provide satisfactory results. For the full cavitation model, the effect of non-condensable gases was neglected. For all the above-mentioned cavitation models, the pressure coefficient distribution was compared to experimental results from the literature.

### **Povzetek**

V prispevku je narejena primerjava med štirimi kavitacijskimi modeli pri numerični napovedi kavitacije na hidrodinamičnem profilu. V ICEM CFD je bila izdelana blokovna strukturirana mreža. V Ansys CFX so se izvedle 2D stacionarne simulacije. Za vse simulacije je bil uporabljen SST turbulentni model s korekcijo, ki jo je uvedel Reboud. Za kavitacijska modela Zwart in Schnerr smo uporabili privzete vrednosti empirični koeficientov. Za full cavitation model in Kunzov kavitacijski model smo vrednosti

<sup>33</sup> Corresponding author: Marko Pezdevšek, University of Maribor, Faculty of Energy Technology, Hočevarjev trg 1, 8270 Krško, E-mail address: [marko.pezdevsek@um.si](mailto:marko.pezdevsek@um.si)

koeficientov določili sami, saj privzete vrednosti niso dale zadovoljivih rezultatov. Za vse štiri zgoraj omenjene kavitacijske modele smo primerjali porazdelitev tlačnega koeficienta z eksperimentalnimi rezultati iz literature.

## 1 INTRODUCTION

Cavitation is a phenomenon that occurs when a combination of low local static pressure and high velocities leads to pressures lower than the vapour pressure. Vapour structures occur in locations where the local pressure is below the vapour pressure.

In some areas, cavitation can be beneficial, for example, in the medical field to remove kidney stones, but in engineering applications such as turbines, pump, and rudders, it is an undesirable effect. Cavitation may cause deterioration in performance, vibrations, and noise. Cavitation erosion occurs when the cavities collapse near the surface of a blade. Cavitation erosion is usually combined with other before mentioned unwanted cavitation effects.

The development of cavitation in liquids can take different patterns. Typical types of cavitation have been classified based on their physical appearance. Some typical cavitation types are presented in Figure 1 and include bubble cavitation, sheet cavitation, vortex cavitation and cloud cavitation.

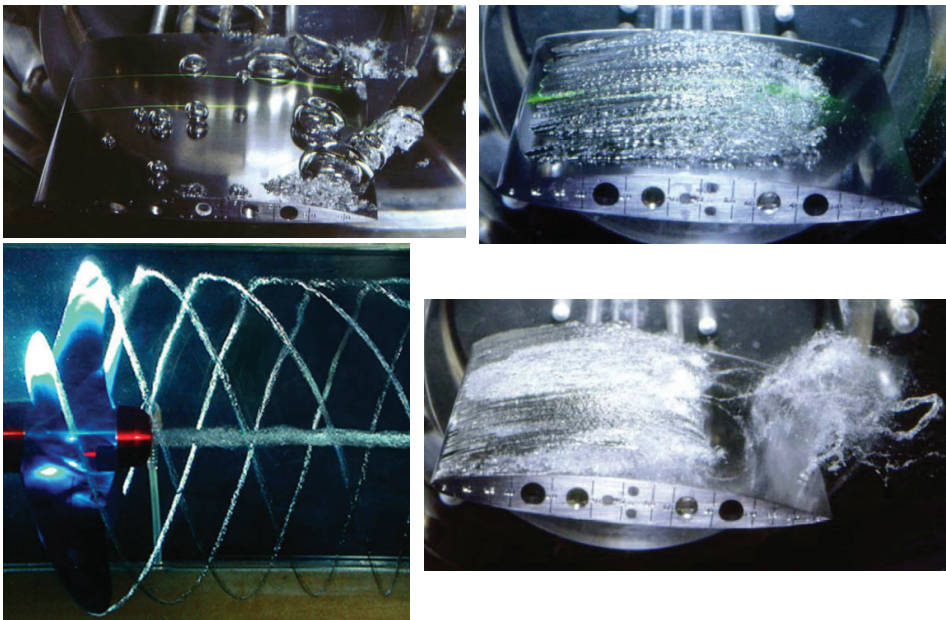


**Figure 1:** Typical cavitation types, upper left travelling bubble cavitation, upper right leading edge sheet cavity, lower left vortex cavitation and lower right cloud cavitation, [1].

To reduce the cost of maintenance and improve the overall performance of a turbine, propellers, pumps or similar machinery, understanding and predicting cavitation and its effects is crucial.

## 2 GEOMETRY AND MESH

The hydrofoil geometry was obtained from [2]. As seen in Figure 2, the chord length of the hydrofoil is 152.4 mm, and the angle of attack is  $1^\circ$ . The size of the domain also shown in Figure 2 is four chord lengths before, six chord lengths after and 2.5 chord length below and above the hydrofoil.

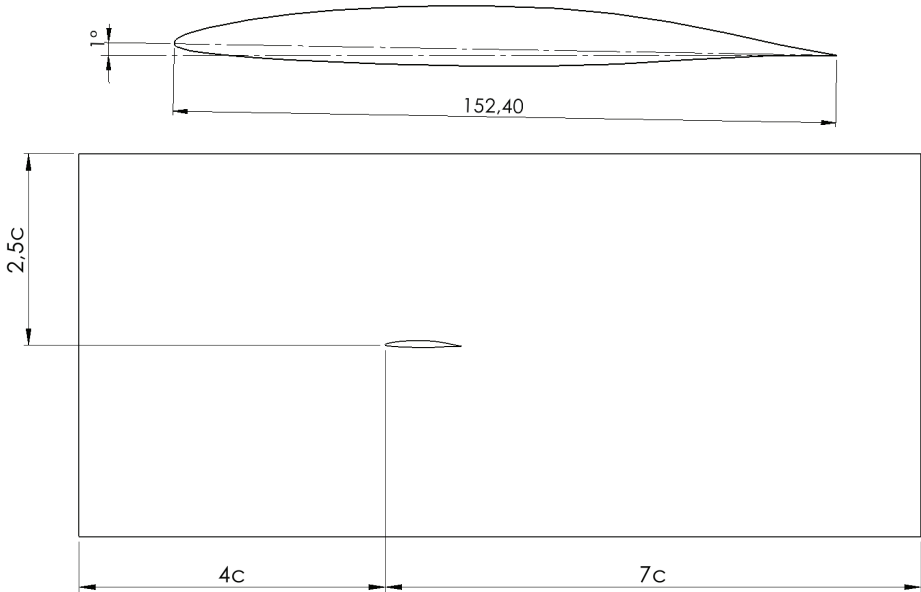


Figure 2: Model dimensions.

For the hydrofoil domain, a blocked structured mesh was created in ICEM CFD. The final mesh consisted of approximately 76,500 elements. The maximum dimensionless value  $y^+$  is below 1, as shown in Figure 3.

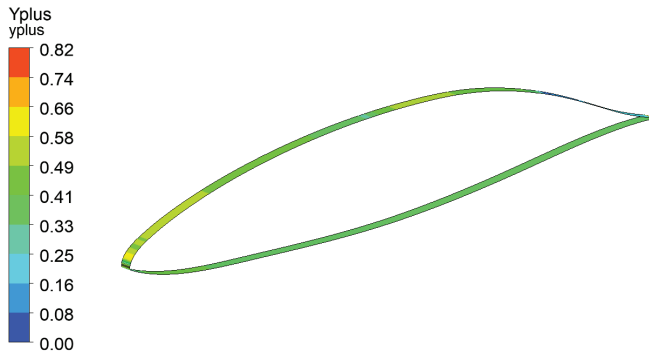
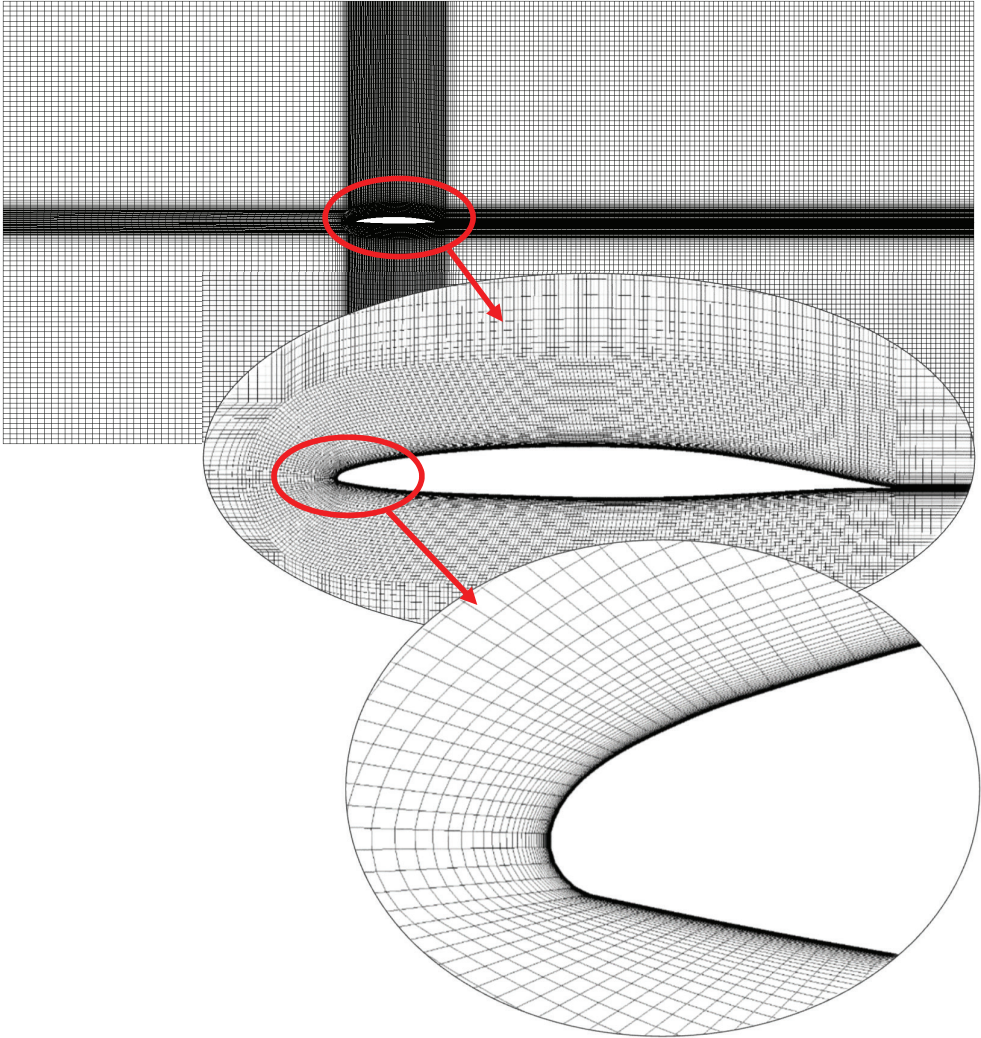


Figure 3: Dimensionless  $y^+$  values on the hydrofoil surface.

The upper image in Figure 4 shows the surface mesh of the model. The middle image shows a magnified cut-out section of the domain, which shows the mesh distribution around the hydrofoil. The bottom image in Figure 4 is a cut out magnified section of the middle image, where mesh distribution near the hydrofoil surface is visible.



**Figure 4:** Surface mesh of the hydrofoil domain (upper image), cut-out magnified section of the upper image (middle section) and cut-out magnified section of the middle image (lower image).

### 3 GOVERNING EQUATIONS, CAVITATION MODELS

In CFX, the homogenous mixture flow is governed by the following set of equations, phases are considered incompressible and share the same velocity field  $\mathbf{U}$ :

Continuity equation:

$$\nabla \cdot \mathbf{U} = \dot{m} \left( \frac{1}{\rho_l} + \frac{1}{\rho_v} \right) \quad (3.1)$$

Where:

- $\mathbf{U}$  – time-averaged mixture velocity [m/s],
- $\dot{m}$  – interphase mass transfer rate due to cavitation [kg/m<sup>3</sup>s],
- $\rho_v$  – vapour density [kg/m<sup>3</sup>],
- $\rho_l$  – liquid density [kg/m<sup>3</sup>].

Momentum equation for the liquid vapour mixture:

$$\frac{\partial(\rho\mathbf{U})}{\partial t} + \nabla \cdot (\rho\mathbf{U}\mathbf{U}) = -\nabla P + \nabla \cdot ((\mu + \mu_t)(\nabla\mathbf{U} + (\nabla\mathbf{U})^T)) \quad (3.2)$$

Where:

- $\rho$  – density of the water-vapour mixture [kg/m<sup>3</sup>],
- $P$  – time averaged pressure [Pa],
- $\mu$  – dynamic viscosity of the water-vapour mixture [kg/m s],
- $\mu_t$  – turbulent viscosity [kg/m s].

Volume fraction equation for the liquid phase.

$$\frac{\partial\gamma}{\partial t} + \nabla \cdot (\gamma\mathbf{U}) = \frac{\dot{m}}{\rho_l} \quad (3.3)$$

Where:

- $\gamma$  – water volume fraction [/].

The water volume fraction and vapour volume fraction are defined as:

$$\gamma = \frac{\text{liquid volume}}{\text{total volume}}; \alpha = \frac{\text{vapour volume}}{\text{total volume}} \quad (3.4)$$

The relation between the water and vapour fraction can be expressed as:

$$\gamma + \alpha = 1 \quad (3.5)$$

The water-vapour mixture density can be defined as:

$$\rho = \gamma\rho_l + (1 - \gamma)\rho_v \quad (3.6)$$

The water-vapour mixture dynamic viscosity is defined as:

$$\mu = \gamma\mu_l + (1 - \gamma)\mu_v \quad (3.7)$$

### 3.1 Turbulence model

Two-equation turbulence models are very widely used, as they offer good compromises between numerical effort and computational accuracy. In the models, the velocity and length scale are solved using separate transport equations. The  $k$ - $\varepsilon$  and  $k$ - $\omega$  two-equation models use the gradient diffusion hypothesis to relate the Reynolds stresses to the mean velocity gradients and the turbulent viscosity. The turbulent viscosity is modelled as the product of a turbulent velocity and turbulent length scale.

The turbulence velocity scale is computed from the turbulent kinetic energy, which is provided from the solution of its transport equation. The turbulent length scale is estimated from two properties of the turbulence field, usually the turbulent kinetic energy and its dissipation rate. The dissipation rate of the turbulent kinetic energy is provided from the solution of its transport equation.

#### 3.1.1 The Shear Stress Transport (SST) Model

The SST turbulence model was proposed by Menter, [3], and is a blend between the  $k$ - $\omega$  model for the region near the surface and  $k$ - $\varepsilon$  model for the outer region. The model consists of a transformation of the  $k$ - $\varepsilon$  model to a  $k$ - $\omega$  formulation. This is achieved by the use of a blending function  $F_1$ .  $F_1$  is equal to one near the surface and decreases to a value of zero outside the boundary layer. [1]

The turbulent kinetic energy  $k$  is defined by:

$$\frac{\partial(\rho k)}{\partial t} + \frac{\partial}{\partial x_j}(\rho U_j k) = \frac{\partial}{\partial x_j} \left[ \left( \mu + \frac{\mu_t}{\sigma_k} \right) \frac{\partial k}{\partial x_j} \right] + P_k - \beta' \rho k \omega + P_{kb} \quad (3.8)$$

Where:

- $P_k$  – production rate turbulence,
- $k$  – turbulent kinetic energy [ $\text{m}^2/\text{s}^2$ ],
- $P_{kb}$  – buoyancy production term.

The specific dissipation rate  $\omega$  is obtained:

$$\frac{\partial(\rho \omega)}{\partial t} + \frac{\partial}{\partial x_j}(\rho U_j \omega) = \frac{\partial}{\partial x_j} \left[ \left( \mu + \frac{\mu_t}{\sigma_\omega} \right) \frac{\partial \omega}{\partial x_j} \right] + \alpha \frac{\omega}{k} P_k - \beta \rho \omega^2 + P_{\omega b} \quad (3.9)$$

Where:

- $\omega$  – specific dissipation rate [ $\text{s}^{-1}$ ],
- $P_{\omega b}$  – buoyancy term.

The model constants are:

- $\beta' = 0.09$ ,
- $\alpha = 5/9$ ,
- $\beta = 0.075$ ,
- $\sigma_k = 2$ ,
- $\sigma_\omega = 2$ .

If we use  $\Phi_1$ ,  $\Phi_2$  and  $\Phi_3$  to represent the terms in the  $k$ - $\varepsilon$ ,  $k$ - $\omega$  and SST model then the coefficients of the SST model are a linear combination of the corresponding coefficients of the underlying models [1]:

$$\Phi_3 = F_1\Phi_1 + (1 - F_1)\Phi_2 \quad (3.10)$$

The turbulent viscosity is modified to account for the transport of the turbulent shear stress. The turbulent viscosity is defined as:

$$\mu_t = \frac{a_1 k}{\rho \max(a_1 \omega, SF_2)} \quad (3.11)$$

Where:

- $S$  – strain rate magnitude [ $s^{-1}$ ],
- $a_1$  – constant (0.31),
- $F_2$  – second blending function.

### 3.1.2 Reboud's correction

Two-equation turbulence models were developed for single phase flows; they tend to overestimate the turbulent viscosity in the region of transition between vapour and liquid phase and damp the unsteadiness of the cavitating regime, [1].

Reboud, [4], proposed a modification of the  $k$ - $\varepsilon$  turbulence model by reducing the turbulent viscosity in order to take into account the suggested two-phase flow effects on the turbulent structures, [1]. The density in the turbulent viscosity equation is now replaced with a density function and is written as:

$$f(\rho) = \rho_v + \frac{(\rho_m - \rho_v)^n}{(\rho_l - \rho_v)^{n-1}} \quad (3.12)$$

Where:

- $\rho_m$  – mixture density [ $kg/m^3$ ],
- $n$  – constant (10).

## 3.2 Cavitation models

The specific interphase mass transfer rate  $\dot{m}'$  was modelled using an appropriate cavitation model. We assume that the specific mass transfer rate is positive if directed from vapour to liquid.

### 3.2.1 Zwart

The Zwart cavitation model was developed by Zwart et al. [5]. The model is based on the multiphase flow equations, with mass transfer due to cavitation appearing as source-and-sink terms in the liquid and vapour continuity equations. The mass transfer rate is derived from a simplified Rayleigh-Plesset model, [5].

$$\dot{m} = \begin{cases} F_{vap} \frac{3r_{nuc}(1-\alpha)\rho_v}{R_B} \sqrt{\frac{2P_v - P}{3\rho_l}} & \text{if } P < P_v \\ F_{cond} \frac{3\alpha\rho_v}{R_B} \sqrt{\frac{2P - P_v}{3\rho_l}} & \text{if } P > P_v \end{cases} \quad (3.13)$$

Where:

$r_{nuc}$  – nucleation site volume fraction [m],

$R_B$  – bubble radius [m],

$P_v$  – vapour pressure [Pa],

$F_{vap}$  – evaporation coefficient [/],

$F_{cond}$  – condensation coefficient [/].

The recommended values for the two coefficients are  $F_{vap} = 50$  and  $F_{cond} = 0.01$ . The recommended values for the nucleation site volume fraction and bubble radius are  $r_{nuc} = 5 \cdot 10^{-4}$  and  $R_B = 10^{-6}$ .

### 3.2.2 Schnerr

Schnerr and Sauer, [6], assumed that the vapour structure is filled with spherical bubbles, which are governed by the simplified Rayleigh Plesset equation. The mass transfer rate in the Schnerr and Sauer model is proportional to  $\alpha(1-\alpha)$ . Moreover, the function  $\frac{\rho_v\rho_l}{\rho}\alpha(1-\alpha)$  has the interesting property that it approaches zero when  $\alpha = 0$  and  $\alpha = 1$  and reaches the maximum in between, [1].

$$\dot{m} = \begin{cases} F_{vap} \frac{\rho_v\rho_l}{\rho} \alpha(1-\alpha) \frac{3}{R_B} \sqrt{\frac{2P_v - P}{3\rho_l}} & \text{if } P < P_v \\ F_{cond} \frac{\rho_v\rho_l}{\rho} \alpha(1-\alpha) \frac{3}{R_B} \sqrt{\frac{2P - P_v}{3\rho_l}} & \text{if } P > P_v \end{cases} \quad (3.14)$$

Where:

$R_B$  – bubble radius [m],

$F_{vap}$  – evaporation coefficient [/],

$F_{cond}$  – condensation coefficient [/].

$$R_B = \left( \frac{\alpha}{1-\alpha} \frac{3}{4\pi n} \right)^{\frac{1}{3}} \quad (3.15)$$

Where:

$n$  – bubble number density [/],

The recommended values for the two coefficients are  $F_{vap} = 1$  and  $F_{cond} = 0.2$ . The recommended values for the bubble number density is  $n = 10^{13}$ .

### 3.2.3 Full cavitation model

The full cavitation model (FCM) was developed by Singhal et al. [7]. The bubble dynamics equation is referred to as a “reduced bubble dynamics formulation” and is derived from the generalized Rayleigh-Plesset equation. It assumes that in most engineering situations, there are plenty of nuclei for the inception of cavitation. The primary focus is on the proper account of bubble growth and collapse, [7].

$$\dot{m} = \begin{cases} C_e \frac{\sqrt{k}}{T} \rho_l \rho_v \sqrt{\frac{2 P_v - P}{3 \rho_l}} (1 - f_v - f_g) & \text{if } P < P_v \\ C_c \frac{\sqrt{k}}{T} \rho_l \rho_l \sqrt{\frac{2 P - P_v}{3 \rho_l}} f_v & \text{if } P > P_v \end{cases} \quad (3.16)$$

Where:

- $f_v$  – vapour mass fraction [/],
- $f_g$  – gas mass fraction [/],
- $T$  – surface tension [N/m],
- $P_v$  – vapour pressure [Pa],
- $C_e$  – empirical coefficient [m/s],
- $C_c$  – empirical coefficient [m/s].

Singhal et al., [8], reported a numerical model using a probability density function approach for accounting for the effects of turbulent pressure fluctuations. The local values of the turbulence pressure fluctuations were defined as:

$$P'_{turb} = 0.39 \rho k \quad (3.17)$$

In [8], computations of time-averaged phase-change rates by the integration of instantaneous rates in conjunction with the assumed probability density function for pressure variation with time were presented. By raising the phase change threshold pressure value, Singhal, [7], proposed a simplified term:

$$P_v = \left( P_{sat} + \frac{P'_{turb}}{2} \right) \quad (3.18)$$

where:

- $P_{sat}$  – saturation pressure [Pa],

The recommended values for the two empirical calibration coefficients are  $C_e = 0.02$  and  $C_c = 0.01$ .

### 3.2.4 Kunz

The Kunz cavitation model is a heuristic model based on work by Merkle et al., [9]. The source term is subdivided into a term related to vaporization and a term related to condensation. The transformation of liquid to vapour is calculated as proportional to the amount by which the

pressure is below the vapour pressure. For the transformation of vapour to liquid, a simplified form of the Ginzburg-Landau potential is employed, [10].

$$\dot{m} = \begin{cases} \frac{C_{prod}\rho_v(\gamma^2 - \gamma^3)}{t_\infty} \\ \frac{C_{dest}\rho_v\gamma \min(0, P - P_v)}{\left(\frac{1}{2}\rho_l U_\infty^2\right) t_\infty} \end{cases} \quad (3.19)$$

where:

$C_{prod}$  – empirical coefficient [ ],  
 $C_{dest}$  – empirical coefficient [ ],  
 $U_\infty$  – free stream velocity [m/s],  
 $t_\infty$  – mean flow time scale [s].

The mean flow time scale is defined as:

$$t_\infty = L/U_\infty \quad (3.20)$$

where:

$L$  – characteristic length scale [m].

The recommended values for the two empirical coefficients are  $C_{prod} = 100$  and  $C_{dest} = 100$ .

## 4 BOUNDARY CONDITIONS AND SIMULATION SETTINGS

For this problem, the following boundary conditions were applied (shown in Figure 5):

- The left surface was specified as an **inlet**, where a normal velocity of 16.91 m/s was defined.
- The right surface was defined as an **outlet**, where a static pressure of 51,957 Pa was defined.
- The top and bottom surfaces were defined as a **free-slip wall**.
- The **symmetry** boundary condition was applied for the side surfaces.
- The hydrofoil surface was defined as a **no-slip wall**.

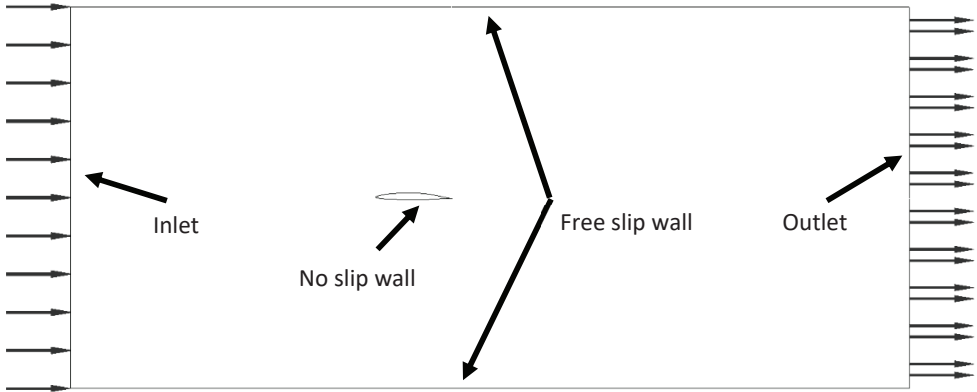


**Figure 5:** Boundary conditions.

The cavitation number is a non-dimensional parameter for cavitating flow and is defined as:

$$\sigma = \frac{p_{ref} - p_v}{0.5\rho_l U_{ref}^2} \quad (4.1)$$

The cavitation number for this case is calculated to 0.34.

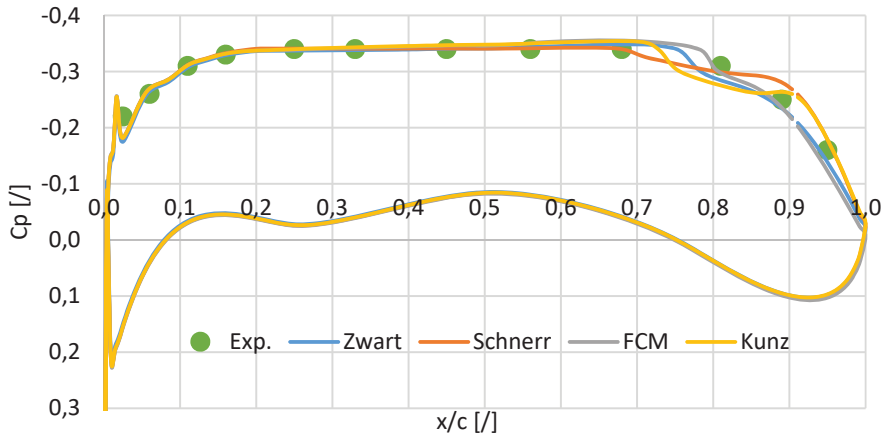
For all four selected cavitation models, steady-state 2D simulations were performed in Ansys CFX. For all cases, the average RMS residuals were set at  $10^{-6}$ , and the SST turbulence model with Reboud's correction was used. For Zwart and Schnerr cavitation models, the recommended values were used for the empirical coefficients. For the FCM cavitation model, we have neglected the effect of non-condensable gases. The two empirical coefficients were set at  $C_e = 1$  and  $C_c = 1$ . For the Kunz cavitation model, the two empirical coefficients were set at  $C_{dest} = 65,000$  and  $C_{prod} = 1800$ . The empirical coefficients used for this study are presented in Table 1.

**Table 1:** Empirical coefficient values for cavitation models used in this study.

Cavitation model	Coefficient values
Zwart	$F_{vap} = 50, F_{cond} = 0.01$
Schnerr	$F_{vap} = 1, F_{cond} = 0.2$
FCM	$C_e = 1, C_c = 1$
Kunz	$C_{dest} = 65,000, C_{prod} = 1800$

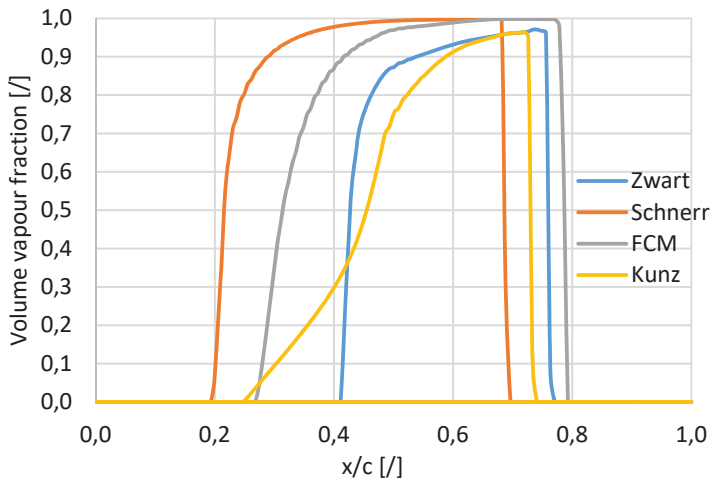
## 5 RESULTS

Figure 6 shows the distribution of the pressure coefficient along the hydrofoil surface for all four selected cavitation models. The pressure coefficient is compared to the experimental results from the literature, [2]. In general, all cavitation models show good agreement with experimental results at  $x/c$  values below 0.7. Above 0.7, the FCM and Zwart cavitation models show the best agreement, while the Kunz cavitation model deviates the most.



**Figure 6:** Pressure coefficient distribution.

The cavitation for the Schnerr model starts at  $x/c=0.2$ ; for the FCM and Kunz model, it starts at approximately  $x/c=0.3$ . For the Zwart model, the cavitation starts at  $x/c=0.4$ . Vapour volume fraction distribution for all cavitation models is seen in Figure 7.



**Figure 7:** Vapour volume fraction distribution.

Figure 8 shows the vapour volume fraction for all cavitation models. The Zwart and FCM models predicted cavitation in a very similar manner, which is also evident from the pressure coefficient distribution. For the Schnerr cavitation model, the values for the vapour volume fraction are higher compared to the other three models.

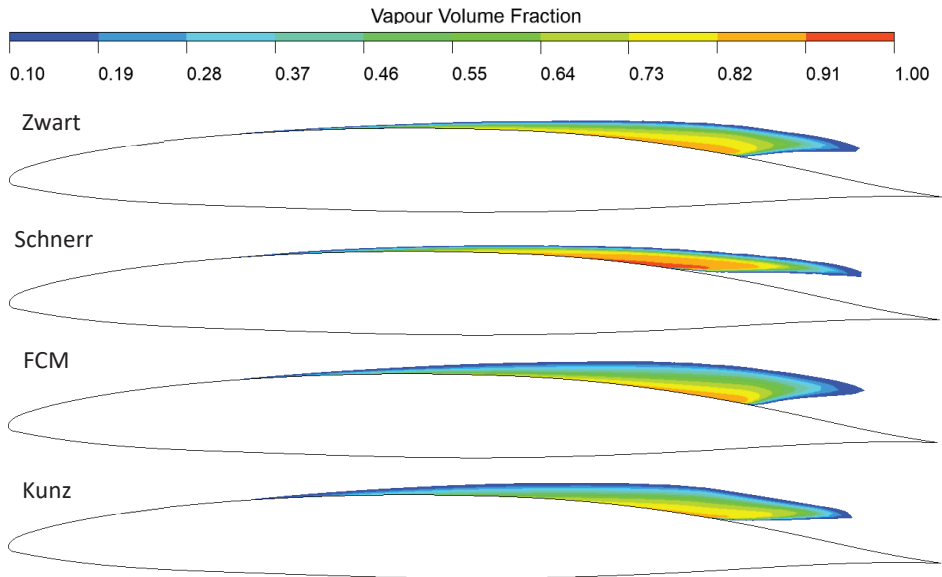


**Figure 8:** Volume vapour fraction for the four selected cavitation models.

## 6 CONCLUSION

Steady-state 2D simulations were performed for a hydrofoil with a chord length of 152.4 mm and an angle of attack of  $1^\circ$ . A velocity of 16.91 m/s was defined, the cavitation number was calculated to 0.34. For all cases, the SST turbulence model with Reboud's correction was used. For Zwart and Schnerr cavitation models, the recommended values were used for the empirical coefficients; the results for the pressure coefficient for both models show good agreement with experimental results. For the FCM cavitation model, we have neglected the effect of non-condensable gases. In this study, the two empirical coefficients were set at  $C_e = 1$  and  $C_c = 1$ . With the set coefficients, the results for the pressure coefficient were in good agreement with the experimental results. For the Kunz cavitation model, the two empirical coefficients were set at  $C_{dest} = 65,000$  and  $C_{prod} = 1800$ . With the set coefficients, the results for the pressure coefficient were in good agreement with the experimental results but compared to other models; the Kunz cavitation model deviates the most. From the results given, it seems that the selected cavitation models in this study can offer similar levels of accuracy, although we should note that with the FCM and Kunz model, the recommended values for the empirical coefficients did not provide satisfactory results.

## References

- [1] **D. Ziru Li:** Assessment of Cavitation Erosion with a Multiphase Reynolds-Averaged Navier-Stokes Method, Wuhan University of Technology, Wuhan, P.R. China, 2012.
- [2] **ANSYS, Inc.:** ANSYS CFX tutorials, 2016
- [3] **F. R. Menter:** Two-Equation Eddy-Viscosity Turbulence Models for Engineering Applications, AIAA Journal, Volume 32, No. 8, August 1994.
- [4] **J. L. Reboud, B. Stutz, O. Coutier-Delgosha:** Two phase flow structure of cavitation: experiment and modeling of unsteady effects, Proceedings of the 3<sup>rd</sup> International Symposium on Cavitation, Grenoble, France, 1998.
- [5] **P. J. Zwart, A. G. Gerber, T. Belamri:** A Two-Phase Flow Model for Predicting Cavitation Dynamics, ICMF 2004 International Conference on Multiphase Flow, Yokohama, Japan, 2004
- [6] **G. H. Schnerr:** Physical and Numerical Modeling of Unsteady Cavitation Dynamics, ICMF-2001, 4th International Conference on Multiphase Flow, New Orleans, USA, 2001
- [7] **A. K. Singhal, H. Li, Y. Jiang:** Mathematical Basis and Validation of the Full Cavitation Model, Journal of Fluids Engineering, 2002
- [8] **A. K. Singhal, N. Vaidya, A. D. Leonard:** Multi-Dimensional Simulation of Cavitating Flows Using a PDF Model for Phase Change, ASME FED Meeting, Vancouver, Canada, 1997.
- [9] **C. L. Merkle, J. Feng, P. Buelow:** Computational modelling of the dynamics of sheet cavitation, Proceedings of 3rd International Symposium on Cavitation, Grenoble, France, 1998.
- [10] **R. F. Kunz, D. A. Boger, D. R. Stinebring, T. S. Chyczewski, J. W. Lindau, H. J. Gibeling, S. Venkateswaran, T. R. Govindan:** Preconditioned Navier-Stokes Method for Two-Phase Flows with Application to Cavitation Prediction, Computers & Fluids 29, 2000.

## Nomenclature

(Symbols)	(Symbol meaning)
$U$	time-averaged mixture velocity
$\dot{m}$	interphase mass transfer rate due to cavitation
$\rho_v$	vapour density
$\rho_l$	liquid density
$\rho$	density of the water-vapour mixture
$P$	time-averaged pressure
$\mu$	dynamic viscosity of the water-vapour mixture
$\mu_t$	turbulent viscosity
$\gamma$	water volume fraction

$P_k$	production rate turbulence
$k$	turbulent kinetic energy
$P_{kb}$	buoyancy production term
$\omega$	specific dissipation rate
$P_{\omega b}$	buoyancy term
$S$	strain rate magnitude
$F_2$	second blending function
$\rho_m$	mixture density
$r_{nuc}$	nucleation site volume fraction
$R_B$	bubble radius
$P_v$	vapour pressure
$F_{vap}$	evaporation coefficient
$F_{cond}$	condensation coefficient
$R_B$	bubble radius
$n$	bubble number density
$f_v$	vapour mass fraction
$f_g$	gas mass fraction
$T$	surface tension
$P_v$	vapour pressure
$C_e$	empirical coefficient
$C_c$	empirical coefficient
$P'_{turb}$	local values of the turbulence pressure fluctuations
$P_{sat}$	saturation pressure
$C_{prod}$	empirical coefficient
$C_{dest}$	empirical coefficient
$U_\infty$	free stream velocity
$t_\infty$	mean flow time scale
$L$	characteristic length scale
$\sigma$	cavitation number



# MODELLING OF MAGNETIC REGENERATOR AND HEAT TRANSFER AGENT IN MICROCHANNELS

## MODELIRANJE MAGNETNEGA REGENERATORJA IN SREDSTVA ZA PRENOS TOPLOTE V MIKROKANALIH

Dorin Botoc<sup>1,3</sup>, Bianca Eliza Oneata<sup>2</sup>, Ionut Rusu<sup>1</sup>, Alexandru Salceanu<sup>1</sup>, Jurij Avsec<sup>3</sup>

**Keywords:** magnetic refrigeration, active magnetic regenerator, magnetocaloric material

### **Abstract**

In this article, a brief introduction of conventional refrigeration is given, followed by a description and history of magnetic refrigeration. The active magnetic regenerator comprises 12 parallel plates of magnetocaloric material (gadolinium (Gd)), through which circulates the heat transfer fluid (water, in this case). At both ends of the regenerator are the heat exchangers. The hot heat exchanger (HHEX) and the cold heat exchanger (CHEX) connects the fluid to the heat sources. The principle of operation of a magnetic refrigeration installation is based on exploiting the magnetocaloric effect from the materials that possess these properties (in this case, Gd).

<sup>3</sup> Corresponding author: Dorin Botoc, Faculty of Electrical Engineering, Energetics and Applied Informatics, Gheorghe Asachi Technical University of Iasi, Romania, E-mail address: [HYPERLINK "mailto:dorinbotoc@yahoo.com"](mailto:dorinbotoc@yahoo.com) dorinbotoc@yahoo.com

<sup>1</sup> Faculty of Electrical Engineering, Energetics and Applied Informatics, Gheorghe Asachi Technical University of Iasi, Romania

<sup>2</sup> University of Strasbourg, Foreign Applied Languages: English - French and Spanish, France

<sup>3</sup> University of Maribor, Faculty of Energy Technology, Laboratory for Thermomechanics, Applied Thermal Energy Technologies and Nanotechnologies, Krško, Slovenia

## **Povzetek**

V tem članku je uvodoma opisano kompresorskega hlajenje, ki mu sledi opis in zgodovina magnetnega hlajenja. Aktivni magnetni regeneratorski obseg 12 vzporednih plošč magnetokaloričnega materiala (gadolinij (Gd)), skozi katerega kroži tekočina za prenos toplote (v tem primeru voda). Na obeh koncih regeneratorskega sta izmenjevalnika toplote. Vroči izmenjevalnik toplote (HHEX) in hladni izmenjevalnik toplote (CHEX) povezujeta tekočino z viri toplote. Načelo delovanja magnetne hladilne naprave temelji na izkoriščanju magnetokaloričnega učinka materialov, ki imajo te lastnosti (v tem primeru Gd).

## **1 BACKGROUND AND INTRODUCTION**

The technology for producing artificial cold based on vapour compression was introduced more than 120 years ago, with small improvements since then, [1]. However, it has reached a technological level at which improvements and performance increases are unlikely. In 2002, they represented 25% of the total electricity consumption in residential areas and 15% of commercial electricity consumption in the US. A difficult problem to solve and quite serious with this type of technology is the refrigerant used; in most cases, it was hydrofluorocarbons (HFC), which when removed from use; this compressible gas is very harmful both for the environment as well as for the ozone layer, [2]. There is a great deal of research on the evolution and development of freons with a much lower pollution level and contribution to global warming. Previously used refrigerants, specifically chlorofluorocarbons (CFCs) and hydrochlorofluorocarbons (HCFCs), have had a devastating effect on the ozone layer, [3].

In this century, with the increased concern regarding global warming and increasing energy consumption, the development of a more energy-efficient refrigeration technology than steam compression is a priority, [4].

Meeting the growing demands of refrigeration and air conditioning while reducing greenhouse gases has led to further research and developments in magnetic refrigeration systems to produce artificial refrigeration. This motivation is the basis for attracting interest in many research centres in Europe, the United States, China, and Japan.

Magnetic refrigeration is based on the magnetocaloric effect of materials with this property, which manifests itself as a change in temperature when subjected to a magnetic field, [5]. This effect is reversible: when the material is no longer under the action of the magnetic field, it returns to its original state. The magnitude of the temperature change depends, in most cases, on the strength of the magnetic field. To obtain maximum energy efficiency and minimize the operating costs of this installation, it is recommended that the magnetic field source use permanent magnets, [6]. As a working agent, magnetic refrigeration uses solid materials: silicon compounds, gadolinium, etc. These materials illustrate the unique and most strongly highlighted property: the magnetocaloric effect, which is manifested by the increase/decrease of the temperature of that material when it is magnetized/demagnetized. This process of obtaining low temperatures (i.e., lower than those of the environment) have thermal conditioning as the main purpose.

## 2 BOUNDARY CONDITION

The modelling and simulation of thermodynamic processes were performed in COMSOL Multiphysics software. The model was inspired by specialized publications and was built using the options offered by this software. The simulated model is assumed to have a mesh model. In Fig. 1, the AMR (active magnetic regenerator) model is presented.

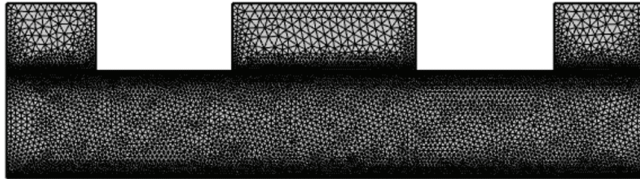


**Figure 1:** COMSOL Multiphysics active magnetic regenerator model used for the simulation

Heat exchangers (HHEX and CHEX) are located at both ends of the AMR. The fluid channel length of the modelled AMR is 300 mm, and the width is 10 mm. The materials were also selected according to the simulations performed in the profile publications, [7]. The AMR uses magnetocaloric gadolinium (Gd) and the assembly was made in the form of parallel plates. Water was used as a heat transfer fluid, [8].

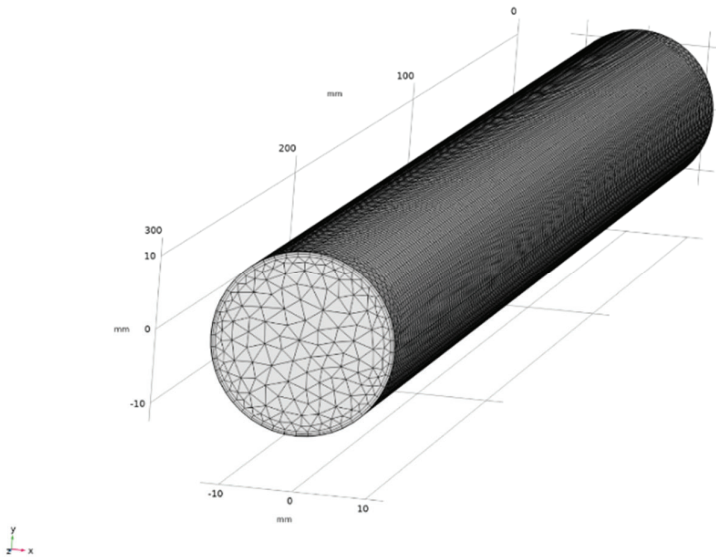


**Figure 2:** Mesh of the fluid channel modelled in COMSOL Multiphysics

### 3 MODELLING AND SIMULATION

This modelling and simulation are mainly based on the study of fluid channels inside the AMR under different magnetization conditions. The modelling was done in COMSOL Multiphysics, and the aim is to increase the efficiency of the regenerator with 12 parallel plates and to use it as a heat-transfer agent.

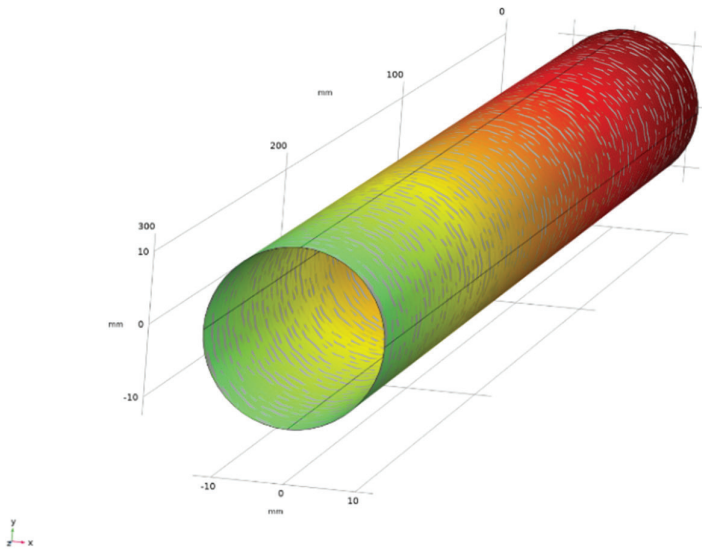


**Figure 3:** 3D model of the fluid channel modelled in COMSOL Multiphysics without Gd plates

The following are the geometric features of this model. The geometry is with parallel plates and microchannels through which the flow of the working agent occurs, [9].

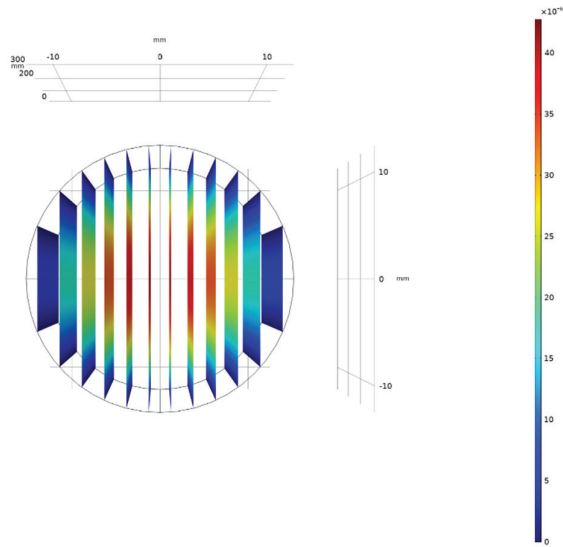


**Figure 4:** 2D model microchannels for heat transfer agent, modelled in COMSOL Multiphysics with Gd plates

The heat transfer fluid used in this AMR model is water, and COMSOL Multiphysics has already implemented Newtonian fluid in its library.

To avoid the oxidation of gadolinium (Gd) plates over time, various compounds can be added to the working agent (water) provided that the physical and thermodynamic properties are not significantly altered. There are different anticorrosive compounds for these types of installations.

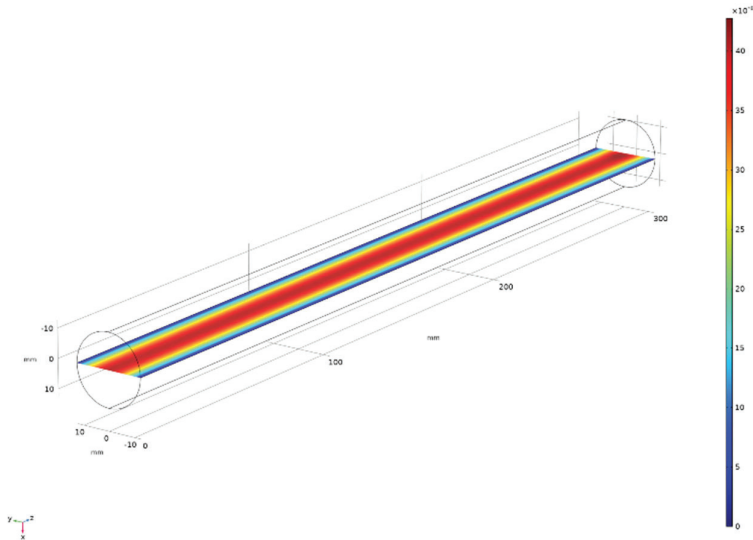


**Figure 5:** 3D model of fluid flow along the length of the Gd plate. inside the canal

When studying the fluid flow, the first characteristic criterion to be considered is the Reynolds number in order to determine the flow regime, [10].

$$Re = \frac{\rho_f v D_h}{\mu_f} \quad (3.1)$$

Where:  $\rho_f, v, \mu_f$  are, density, speed and dynamic viscosity of the heat transfer fluid, and  $D_h$  is the hydraulic diameter.

The hydraulic diameter represents the characteristic length of the fluid flow and can be defined as:

$$D_h = \frac{4A_c}{P} \quad (3.2)$$

Where:  $A_c$  is the flow section and  $P$ , wetted perimeter

## 4 RESULTS AND DISCUSSION

When the heat transfer agent flows in the X direction, having been in contact with the Gd plates, which have a different temperature, the so-called hydrodynamic boundary layer appears near the solid wall. The profile below is circular, so it is possible to define an average Reynolds number, [11-12]. It can be seen how the fluid temperature drops from a maximum in the centre of the microchannel to almost zero to the boundary layer of the channel wall.

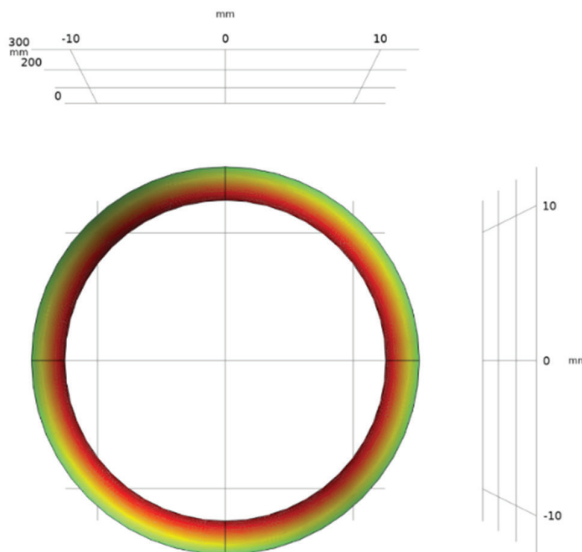


**Figure 6:** 2D model of the fluid channel temperature modelled in COMSOL Multiphysics

Magnetization, specific heat and adiabatic variation of the temperature of the magnetocaloric material Gd varies depending on two essential parameters: temperature and the applied magnetic field, [13].

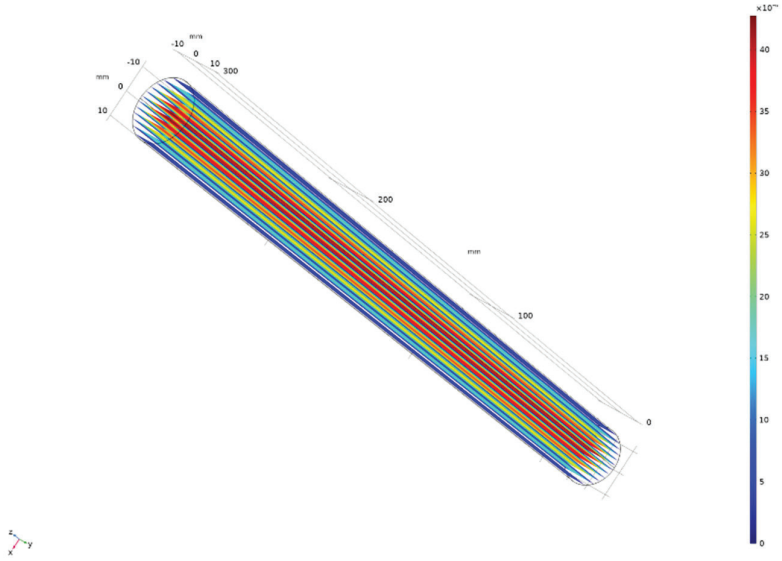


**Figure 7:** 3D model of the fluid channel temperature modelled in COMSOL Multiphysics with 12 parallel Gd plates

In this way, a direct application of the adiabatic temperature variation on the parallel Gd plates is obtained. At each step, the temperature of the plates made of magnetocaloric material Gd varies according to the equation below, [14]:

$$T = T(t) + \Delta T_{ad}(T(t), \mu_0 H(t), \mu_0 H(t + \Delta t)) \quad (4.1)$$

The internal energy for the plates of magnetocaloric material Gd can be written as follows:

$$U = U(S, V, H) \quad (4.2)$$

And in differential form:

$$dU = TdS - pdV - MdH \quad (4.3)$$

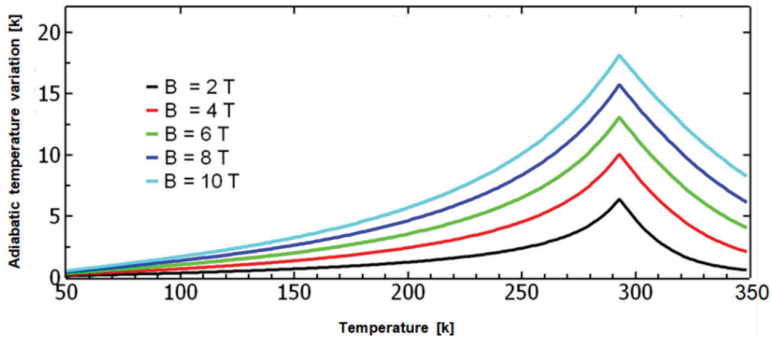
For the operation of the magnetic refrigeration system at constant pressure, the enthalpy can be defined as:

$$G = U - TS + pV - MH \quad (4.4)$$

And in differential form:

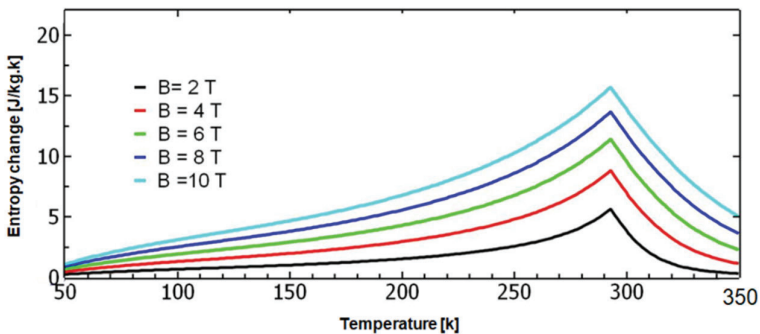
$$dG = Vdp - SdT - MdH \quad (4.5)$$

Fig.9 shows the variation of the adiabatic temperature of the gadolinium for a variation of the magnetic field from 2T (black line) to the maximum intensity of the magnetic field of 10T (light blue line). We can see the evolution of the values of the adiabatic temperature variation of gadolinium as a function of temperature.



**Figure 8:** Variation of the adiabatic temperature of the Gd plates made with the MatLab algorithm

In Fig. 10, we can see the evolution of the entropy change of the Gd plates depending on the applied magnetic field. This variation of the magnetic field is made from 2T (black curve) to 10T (light blue curve). For all values of magnetic intensity, the evolution is slow at the beginning until the maximum value of 15 J/kgK, after which it is slowly decreasing. We observed that the contribution of electron entropy is negligible, and after Curie temperatures, the magnetocaloric material gadolinium becomes paramagnetic, [15].



**Figure 9:** Evolution of the entropy change of Gd plates. performed in the MatLab algorithm

In Fig. 10 (below), one can see the 3D model simulated in COMSOL Multiphysics of the fluid channel in AMR with 12 gadolinium plates (Gd.)

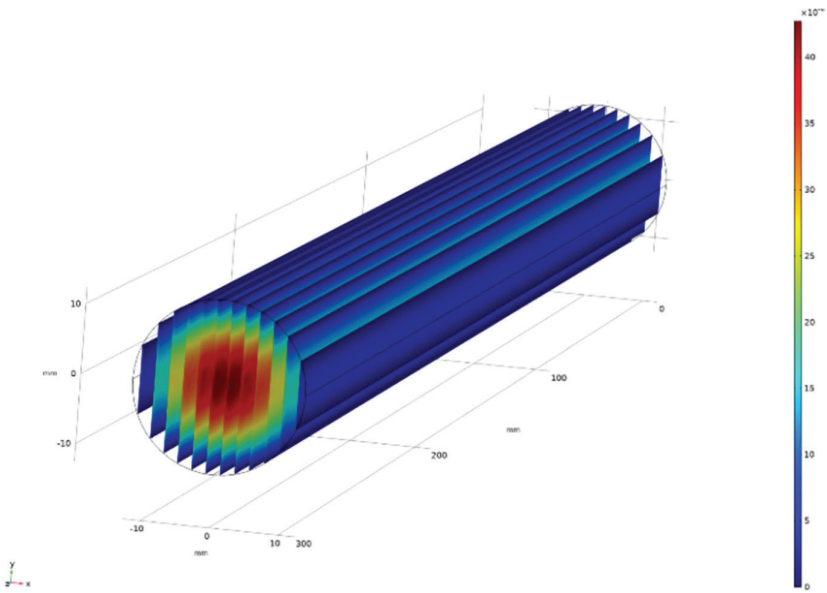


**Figure 10:** 3D model of the fluid channel for magnetic regenerator, modelled in COMSOL Multiphysics

## 5 CONCLUSIONS AND PERSPECTIVES

The first part of this paper presented the basic concepts of magnetic refrigeration and its definitions. In recent years, interest in this technology has grown considerably, due to the advantages we have shown. Then, we explained how this technology works based on magnetocaloric materials, in our case, gadolinium (Gd), which remains the reference material in this field due to its specific properties. In addition to the magnetocaloric material that is part of the AMR, the heat transfer fluid and the location of the parallel plates are quite important components. In Fig. 1 an AMR with 12 parallel gadolinium plates (Gd) was modelled. Fig. 2 shows the fluid channel mesh; 12 parallel gadolinium plates (Gd) were used. Fig. 10 shows the 3D model of the 12 gadolinium plates (Gd) in COMSOL Multiphysics, placed in parallel and water was used as a working agent. The advantages of this technology were shown with the possibility of further study of different types of AMRs: with gadolinium powder (Gd), with gadolinium spheres (Gd) and the accentuation of the modelling of heat transfer, magnetism, and convective transport of the working agent.

## References

- [1] **Sergiu Lionte:** *Caractérisation, étude et modélisation du comportement thermomagnétique d'un dispositif de réfrigération magnétique à matériaux non linéaires et point de Curie proche de la température ambiante*, PhD Thesis, 2015
- [2] **Brown, G. V.:** *Magnetic heat pumping near room temperature*, Journal of Alloys and Compounds, 47(8), 3673-3680, 1976
- [3] **Kitanovski, A. Egolf:** *Thermodynamics of magnetic refrigeration*, International journal of refrigeration, 29(3-12), 3-21, 2005
- [4] **J Tusek, A Kitanovski, A Flisar et al:** *Active magnetic regenerator (AMR) experimental devices*, în Fifth IIF-IIR international conference on magnetic refrigeration at room temperature, Thermag V, Grenoble, France, 2012
- [5] **Nellis, G., Engelbrecht, K., Klein, S., Zimm, C., and Russek, S.:** *Model and Evaluation Tools for Assessing Magnetocaloric Effect for Space Conditioning and Refrigeration Applications*, 2004
- [6] **Tishin, A. M., Gschneidner, K. A., and Pecharsky, V. K.:** *Magnetocaloric effect and heat capacity in the phase-transition region*, Physical Review B, 59(1), 503-511, 1999
- [7] **Tishin, A., and Spichkin, Y.:** *The Magnetocaloric Effect and its Applications.*, Institute of Physics Publishing, 2003
- [8] **Kirol LD, Mills JI:** *Numerical analysis of thermomagnetic generators*, J Appl Phys 56:824–828, 1984
- [9] **Salomon D:** *Thermomagnetic mechanical heat engines*, J Appl Phys 65:3687–3693, 1989
- [10] **Pecharsky VK, Gschneidner KA Jr:** *Effect of alloying on the giant magnetocaloric effect of Gd<sub>5</sub>(Si<sub>2</sub>Ge<sub>2</sub>)*, J Magn Magn Mater 167:179–184, 1997
- [11] **Sergiu Lionte et al.:** *Numerical analysis of a reciprocating active magnetic regenerator*, Applied Thermal Engineering, ELSEVIER, 2014
- [12] **C Vasile, C Muller:** *Innovative design of a magnetocaloric system*, Int J Refrig, nr. 29:1318-1326, 2006
- [13] **C Vasile, C Muller:** *A new system for a magnetocaloric refrigerator*, în First IIF-IIR international conference on magnetic refriation at room temperature, Thermag I, Montreux, Switzerland, 2005
- [14] **KW Lipso, KK Nilesen, DV Christensen et al:** *Measuring the effect of demagnetization in stacks of gadolinium plate using the magnetocaloric effect*, J Magn Magn Mater, nr. 323:3027-3032, 2011
- [15] **C Aprea, A Grego, A Maiorino et al:** *Initial experimental results from a rotary permanent magnet magnetic refrigerator*, Int J Refrig, vol. 43, nr. 111-122, 2014

## **Nomenclature**

<b>(Symbols)</b>	<b>(Symbol meaning)</b>
AMR	active magnetic regenerator
Gd	gadolinium material
HHEX	hot heat exchanger
CHEX	cold heat exchanger





# MAIN TITLE OF THE PAPER SLOVENIAN TITLE

*Author<sup>1</sup>, Author<sup>2</sup>, Corresponding author<sup>✉</sup>*

Keywords: (Up to 10 keywords)

## **Abstract**

Abstract should be up to 500 words long, with no pictures, photos, equations, tables, only text.

## **Povzetek**

(Abstract in Slovenian language)

**Submission of Manuscripts:** All manuscripts must be submitted in English by e-mail to the editorial office at [jet@um.si](mailto:jet@um.si) to ensure fast processing. Instructions for authors are also available online at <http://www.fe.um.si/en/jet/author-instructions.html>.

**Preparation of manuscripts:** Manuscripts must be typed in English in prescribed journal form (MS Word editor). A MS Word template is available at the Journal Home page.

A title page consists of the main title in the English and Slovenian language; the author(s) name(s) as well as the address, affiliation, E-mail address, telephone and fax numbers of author(s). Corresponding author must be indicated.

**Main title:** should be centred and written with capital letters (ARIAL bold 18 pt), in first paragraph in English language, in second paragraph in Slovenian language.

**Key words:** A list of 3 up to 6 key words is essential for indexing purposes. (CALIBRI 10pt)

**Abstract:** Abstract should be up to 500 words long, with no pictures, photos, equations, tables, - text only.

**Povzetek:** - Abstract in Slovenian language.

**Main text** should be structured logically in chapters, sections and sub-sections. Type of letters is Calibri, 10pt, full justified.

---

✉ Corresponding author: Title, Name and Surname, Organisation, Department, Address, Tel.: +XXX x xxx xxx, E-mail address: x.x@xxx.xx

<sup>1</sup> Organisation, Department, Address

<sup>2</sup> Organisation, Department, Address

Units and abbreviations: Required are SI units. Abbreviations must be given in text when first mentioned.

Proofreading: The proof will be send by e-mail to the corresponding author in MS Word's Track changes function. Corresponding author is required to make their proof corrections with accepting or rejecting the tracked changes in document and answer all open comments of proof reader. The corresponding author is responsible to introduce corrections of data in the paper. The Editors are not responsible for damage or loss of submitted text. Contributors are advised to keep copies of their texts, illustrations and all other materials.

The statements, opinions and data contained in this publication are solely those of the individual authors and not of the publisher and the Editors. Neither the publisher nor the Editors can accept any legal responsibility for errors that could appear during the process.

Copyright: Submissions of a publication article implies transfer of the copyright from the author(s) to the publisher upon acceptance of the paper. Accepted papers become the permanent property of "Journal of Energy Technology". All articles published in this journal are protected by copyright, which covers the exclusive rights to reproduce and distribute the article as well as all translation rights. No material can be published without written permission of the publisher.

Chapter examples:

## 1 MAIN CHAPTER

**(Arial bold, 12pt, after paragraph 6pt space)**

### 1.1 Section

**(Arial bold, 11pt, after paragraph 6pt space)**

#### 1.1.1 Sub-section

**(Arial bold, 10pt, after paragraph 6pt space)**

Example of Equation (lined 2 cm from left margin, equation number in normal brackets (section. equation number), lined right margin, paragraph space 6pt before in after line):

$$\text{Equation} \tag{1.1}$$

Tables should have a legend that includes the title of the table at the top of the table. Each table should be cited in the text.

Table legend example:

***Table 1: Name of the table (centred, on top of the table)***

Figures and images should be labelled sequentially numbered (Arabic numbers) and cited in the text – Fig.1 or Figure 1. The legend should be below the image, picture, photo or drawing.

Figure legend example:

**Figure 1:** *Name of the figure (centred, on bottom of figure, photo, or drawing)*

## References

- [1] **N. Surname:** *Title*, Journal Title, Vol., Iss., p.p., Year of Publication
- [2] **N. Surname:** *Title*, Publisher, Year of Publication
- [3] **N. Surname:** *Title* [online], Publisher or Journal Title, Vol., Iss., p.p., Year of Publication. Available: website (date accessed)

Examples:

- [1] **J. Usenik:** *Mathematical model of the power supply system control*, Journal of Energy Technology, Vol. 2, Iss. 3, p.p. 29 – 46, 2009
- [2] **J. J. DiStefano, A.R. Stubberud, I. J. Williams:** *Theory and Problems of Feedback and Control Systems*, McGraw-Hill Book Company, 1987
- [3] **T. Žagar, L. Kegel:** *Preparation of National programme for SF and RW management taking into account the possible future evolution of ERDO* [online], Journal of Energy Technology, Vol. 9, Iss. 1, p.p. 39 – 50, 2016. Available: [http://www.fe.um.si/images/jet /Volume 9\\_Issue1/03-JET\\_marec\\_2016-PREPARATION\\_OF\\_NATIONAL.pdf](http://www.fe.um.si/images/jet /Volume 9_Issue1/03-JET_marec_2016-PREPARATION_OF_NATIONAL.pdf) (7. 10. 2016)

Example of reference-1 citation: In text [1], text continue.

## Nomenclature

(Symbols)	(Symbol meaning)
t	time



ISSN 1855-5748



9 771855 574008